The Astrophysical Journal, 890:58 (33pp), 2020 February 10 https://doi.org/10.3847/1538-4357/ab6a10

Gauss–Bonnet Inflation after Planck2018

Narges Rashidi[1,2] and Kourosh Nozari[1]
[1] Department of Theoretical Physics, Faculty of Basic Sciences, University of Mazandaran, P.O. Box 47416-95447, Babolsar, Iran; n.rashidi@umz.ac.ir
[2] Research Institute for Astronomy and Astrophysics of Maragha (RIAAM), P.O. Box 55134-441, Maragha, Iran; knozari@umz.ac.ir
Received 2019 September 2; revised 2020 January 6; accepted 2020 January 8; published 2020 February 12

Abstract

We study the primordial perturbations and reheating process in the models where the Gauss–Bonnet (GB) term is nonminimally coupled to the canonical and noncanonical (DBI and tachyon) scalar fields. We consider several potentials and GB coupling terms as power-law, dilaton-like, cosh-type, E-model, and T-model. To seek the observational viability of these models, we study the scalar perturbations numerically and compare the results with the Planck2018 TT, TE, EE+lowE+lensing+BK14+BAO joint data at 68% CL and 95% CL. We also study the tensor perturbations in confrontation with the Planck2018 TT, TE, EE+lowE+lensing+BK14+BAO+ LIGO, and Virgo2016 joint data at 68% CL and 95% CL. In this regard, we obtain some constraints on the GB coupling parameter β. Another important process in the early universe is the reheating phase after inflation, which is necessary to reheat the universe for subsequent evolution. In this regard, we study the reheating process in these models and find some expressions for the e-folds number and temperature during that era. Considering that from Planck TT, TE, EE+lowEB+lensing data and BICEP2/Keck Array 2014, based on the ΛCDM+$r+\frac{dn_s}{d\ln k}$ model, we have $n_s = 0.9658 \pm 0.0038$ and $r < 0.072$, we obtain some constraints on the e-folds number and temperature. From the values of the e-folds number and the effective equation of state and also the observationally viable value of the scalar spectral index, we explore the capability of the models in explaining the reheating phase.

Unified Astronomy Thesaurus concepts: Inflationary universe (784); Observational cosmology (1146); Early universe (435)

1. Introduction

One simple way to solve some problems of the standard model of cosmology is to consider a single canonical scalar field (inflation) with a flat potential leading to the slow-roll of the inflation. The slow-rolling of the inflation causes enough exponential expansion of the early universe. The primordial perturbations in this single-field model would have adiabatic, scale-invariant, and Gaussian-dominant modes (Guth 1981; Albrecht & Steinhard 1982; Linde 1982, 1990; Lidsey et al. 1997; Liddle & Lyth 2000; Riotto 2002; Maldacena 2003; Lyth & Liddle 2009). However, some cosmologists are interested in the extended inflation models predicting the non-Gaussian distributed perturbations (Maldacena 2003; Bartolo et al. 2004; Chen 2010; De Felice & Tsujikawa 2011a, 2011b; Nozari & Rashidi 2013a, 2016a; Nojiri & Odintsov 2011; Nojiri et al. 2017).

Thinking over the very early time in the history of the universe, approaching the Planck scale, and studying that epoch, it seems necessary to incorporate some quantum corrections into the Einstein gravity. The quantum theory of gravity at the low-energy limit leads to the Einstein theory of gravity (Burgess 2004). There is this belief that, as a promising candidate for the quantum gravity, we can consider string theory. To import the quantum effects of gravity by using the higher-order curvature correction to the gravitational action, string theory suggests to consider the Gauss–Bonnet (GB) term (Gross & Sloan 1987). This term is a quadratic term defined by

$$\mathcal{L}_{\rm GB} = R_{\rm abcd}\, R^{\rm abcd} - 4R_{\rm ab}\, R^{\rm ab} + R^2\,, \qquad (1)$$

which is part of Lovelock's theorem (Lovelock 1971), and its role in the dynamics of the early universe is significant (Boulware & Deser 1985; Zwiebach 1985). By adding this term to the action of the theory, which makes the action ghost-free, we do not face the unitarity problem. However, it turns out that when we deal with the GB term in dimensions fewer than five, this term behaves just like a topological term and therefore has no influence on the background dynamics. To import the GB effect on the background dynamics, one way is to consider the GB term in higher dimensions (Andrew et al. 2007; Bamba et al. 2007; Brown 2007; Nozari & Fazlpour 2008; Nozari & Rashidi 2009a, 2009b, 2009c). Another way, if we look for the GB effect in four dimensions, is to couple it nonminimally to a scalar field or adopt a function of the GB term in the four-dimensional action (Nojiri et al. 2005, 2007; Nojiri & Odintsov 2005; Guo & Schwarz 2009, 2010; Koh et al. 2014, 2017; Elizalde et al. 2018; Odintsov & Oikonomou 2018; Odintsov et al. 2019; Wu et al. 2018; Nojiri et al. 2019). Among the work done on this issue, we focus on the models in which the GB term is nonminimally coupled to the scalar field in the theory. Some authors have studied these types of GB inflation models and found some interesting observational results. In this regard, the GB inflation models with power-law, inverse power-law, and exponential potentials and GB coupling have been studied (Guo & Schwarz 2009, 2010; Jiang et al. 2013; Koh et al. 2014; Odintsov & Oikonomou 2018), and the results have been compared with different data sets such as *Wilkinson Microwave Anisotropy Probe* 5 yr (Komatsu et al. 2009), Planck+WP (Ade et al. 2014b), Planck+WP+highL +BICEP2 (Ade et al. 2014a), and BICEP2/Keck Array (Ade et al. 2016) data.

Another interesting case in studying the inflation models is the idea of a "cosmological attractor." In this regard, α-attractor models are one class of the models incorporating the idea of cosmological attractors that have attracted a lot of attention

(Ferrara et al. 2013; Kallosh et al. 2013, 2014a, 2014b, 2016; Cecotti & Kallosh 2014; Kaiser & Sfakianakis 2014; Joseph et al. 2015a, 2015b; Linde 2015; Odintsov & Oikonomou 2016; Shahalam et al. 2018; Nozari & Rashidi 2018; Rashidi & Nozari 2018). In the α-attractor models, the E-model potential is given by $V \sim \left[1 - \exp\left(-\sqrt{\frac{2\kappa^2}{3\alpha}}\,\phi\right)\right]^{2n}$. It is interesting to consider the GB coupling term as E-model and study the inflation and perturbations (Nozari & Rashidi 2017; Yi et al. 2018). T-model potential in the α-attractor models is given by $V \sim \tanh^{2n}(\frac{\kappa\phi}{\sqrt{6\alpha}})$. It is also possible to take the GB term in the inflation models as the T-model, which gives cosmologically viable results (Yi et al. 2018).

On the other hand, we should notice that the scalar field responsible for the inflation can be a canonical as well as a noncanonical scalar field such as tachyon (Sen 1999, 2002a, 2002b) or Dirac–Born–Infeld (DBI; Alishahiha et al. 2004; Silverstein & Tong 2004). Studying the inflation in tachyon and DBI models gives interesting results (Cardenas 2006; Spalinski 2007; Deshamukhya & Panda 2009; Campo et al. 2009; Mizuno & Koyama 2010; Nozari & Rashidi 2013a, 2013b, 2019; Rashidi et al. 2018). In this regard, one can consider the coupling between these noncanonical scalar fields and the GB term. Also, it is possible in the GB inflation models to consider the nonminimal coupling or nonminimal derivative coupling between the scalar field and gravity (or any generalized inflationary models; De Felice & Tsujikawa 2011a; Nozari & Rashidi 2016b).

Although a lot of works have been done on the GB inflation issue, the observational viability of those models depends on the newest data released at any time. Recently, the Planck2018 Collaboration has released the new results (Akrami et al. 2018; Aghanim et al. 2018). From Planck2018 TT, TE, EE+lowE +lensing data,[3] based on the ΛCDM $+r + \frac{dn_s}{d\ln k}$ model, which supports quasi–de Sitter expansion of the universe during the inflation epoch, we have constraints on the scalar spectral index and tensor-to-scalar ratio as $n_s = 0.9647 \pm 0.0044$ and $r < 0.16$ (Akrami et al. 2018). However, when we consider the joint data of Planck2018, BAO, and BICEP2/Keck Array 2014, which means Planck2018 TT, TE, EE+lowE+lensing +BAO +BK14 data (hereafter base data), we have $n_s = 0.9658 \pm 0.0038$ and $r < 0.072$ (Akrami et al. 2018). By these new constraints on the perturbation's parameters, some inflation models might be ruled out and the constraints on some parameters of the other inflation models might be changed. Another piece of information that the Planck2018 team gives us is on the tensor spectral index. Planck2018 gives the constraint on the tensor spectral index as $-0.62 < n_T < 0.53$ with $r < 0.080$, obtained from Planck2018 TT, TE, EE +lowE+lensing+BK14+BAO+LIGO and Virgo2016 joint data (hereafter, base+GW data; Akrami et al. 2018). It seems that, analyzing and studying the tensor part of the perturbations in the GB models, which has been less studied before, gives us some more information about the inflation models.

[3] TT, TE, and EE refer to temperature auto-power spectrum, temperature-E-mode cross-power spectrum, and E-mode polarization auto-power spectrum, respectively. Planck2018 TT, TE, EE+lowEB denotes the combination of the likelihood at multipole $l \geqslant 30$ using TT, TE, and EE spectra, the low-l SimAll EE likelihood, and the low-l temperature Commander likelihood (Akrami et al. 2018). When Planck2018 B-mode information is included, the abbreviation is Planck TT, TE, EE+lowEB. Also, BK14 refers to BICEP2/Keck Array 2014 data and BAO denotes baryon acoustic oscillations.

Another important issue in studying the inflation models is the reheating process after inflation. As long as the potential is sufficiently flat, meaning that the slow-roll parameters ϵ and η are very small, the universe inflates exponentially. When one of the slow-roll parameters meets unity, the inflation ends and the inflation field rolls down to the minimum of the potential. By reaching the minimum of the potential, inflation starts oscillating about that minimum and losing the energy. In this regard, according to the physics of particles creation and nonequilibrium phenomena, it decays into the plasma of the relativistic particles and the universe becomes radiation dominated (Abbott et al. 1982; Albrecht et al. 1982; Dolgov & Linde 1982). There are other interesting but complicated reheating scenarios, including the nonperturbative processes, proposed by some authors. Some examples of the nonperturbative reheating scenarios are the parametric resonance decay (Traschen & Brandenberger 1990; Kofman et al. 1994, 1997), tachyonic instability (Greene et al. 1997; Felder et al. 2001a, 2001b; Dufaux et al. 2006; Shuhmaher & Brandenberger 2006; Abolhasani et al. 2010), and the instant preheating (Felder et al. 1999). To analyze the reheating process, we focus on two important parameters $N_{\rm rh}$ (e-folds number) and $T_{\rm rh}$ (temperature) in this phase. Studying these parameters gives us some more constraints on the model's parameters space (Dai et al. 2014; Cai et al. 2015; Cook et al. 2015; Munoz & Kamionkowski 2015; Ueno & Yamamoto 2016). The effective equation-of-state parameter, $\omega_{\rm eff}$, is another important parameter in exploring the reheating phase. For a massive inflation, domination of the potential over the kinetic energy leads to $\omega_{\rm eff} = -1$, and domination of the kinetic energy over the potential leads to $\omega_{\rm eff} = 1$. Given that at the initial epoch of the reheating process the massive inflation oscillates with frequency much larger than the expansion rate, the averaged effective pressure at that epoch is zero. This means that, at the initial epoch of the reheating phase, we can assume $\omega_{\rm eff} = 0$, which corresponds to the equation-of-state parameter of the dust matter. Also, at the end of the reheating phase, we have $\omega_{\rm eff} = \frac{1}{3}$. Therefore, exploring the effective equation of state gives us some more information about the reheating phase.

Based on these preliminaries, in this paper we focus on the GB inflation models and reconsider them to seek their observational viability in confrontation with base and base +GW data sets. In this regard, in Section 2, we study the inflation and perturbations in the general GB model. In Section 3, we consider the GB model with a canonical scalar field. In this respect, by adopting power-law potential and two types of GB coupling as inverse power-law and dilaton-like couplings, we obtain the tensor-to-scalar ratio and scalar and tensor spectral indices and investigate the observational viability of the model. In Section 4, we perform analysis on the GB natural inflation, in which the potential of the scalar field is cos-type and the GB coupling is inverse of cos. The GB α-attractor is studied in Section 5, with both E-model and T-model potential and GB coupling. In Section 6, we analyze a GB inflation in which the inflation is the tachyon field. By adopting power-law potential and both inverse power-law and dilaton-like GB coupling, we check the observational viability of this model. The DBI GB inflation, with power-law potential, inverse power-law DBI field, and both inverse power-law and dilaton-like GB coupling, is explored in Section 7. The reheating process after inflation for the GB model with a canonical scalar field is investigated in Section 8. In this regard,

we obtain some expressions for the e-folds number and temperature during the reheating process. By using the observational constraint on the scalar spectral index, we find some constraints on $N_{\rm rh}$ and $T_{\rm rh}$. We also study the effective equation of state during this process. In Section 9, we investigate the reheating phase in the GB model with the tachyon field. The reheating phase in the DBI GB model is studied in Section 10. In Section 11, we present a summary of the paper. We emphasize that although the GB inflation models have been studied in several papers, the tensor perturbations in the GB models have been less studied. Also, the reheating phase is an interesting issue in studying the inflation models, which for most of the models we study here have never been studied.

2. The General GB Inflation

In this section, we present the inflation and perturbations in a cosmological model in which a GB term is nonminimally coupled to the scalar field. In this setup, the action is given by

$$S=\int d^4x\sqrt{-g}\left[\frac{1}{2\kappa^2}R+P(X,\,\phi)-\mathcal{G}(\phi)\mathcal{L}_{\rm GB}\right], \tag{2}$$

where ϕ is the scalar field, R is the Ricci scalar, $\mathcal{L}_{\rm GB}$ is the GB term with the coupling function $\mathcal{G}(\phi)$, and $X=-\frac{1}{2}g^{\mu\nu}\partial_\mu\phi\,\partial_\nu\phi$. Action (2) in a spatially flat FRW metric gives the following background equations:

$$H^2=\frac{\kappa^2}{3\mathcal{F}}[-P+2XP_{,X}+24H^3\dot{\mathcal{G}}], \tag{3}$$

$$\begin{aligned}&(P_X+2XP_{,XX})\ddot{\phi}+(3HP_{,X}+\dot{\phi}P_{,\phi X})\\&\dot{\phi}-P_{,\phi}+24H^4\mathcal{G}'+24H^2\dot{H}\mathcal{G}'=0,\end{aligned} \tag{4}$$

where the subscript "," shows derivative with respect to the corresponding parameter, a dot denotes a derivative with respect to the cosmic time, and a prime shows a derivative with respect to the scalar field.

The slow-roll parameters ϵ and η, defined as

$$\epsilon=-\frac{\dot{H}}{H^2},\quad \eta=-\frac{1}{H}\frac{\ddot{H}}{\dot{H}}, \tag{5}$$

under the conditions $\epsilon\ll 1$ and $|\eta|\ll 1$ show the inflation phase. In this extended setup, with GB correction, the slow-roll limits are $\ddot{\phi}\ll|3H\dot{\phi}|$, $\dot{\phi}^2\ll V(\phi)$, $H\dot{\mathcal{G}}\ll\kappa^{-2}$, and $P_{,X}X\ll\kappa^{-2}H^2$ (see Guo & Schwarz 2010; Bruck & Longden 2016; Nozari & Rashidi 2016b).

The e-folds number, which is defined as

$$N=\int_{t_{\rm hc}}^{t_f}H\,dt, \tag{6}$$

in this model and within the slow-roll conditions is given by

$$N=\int_{\phi_{\rm hc}}^{\phi_f}\frac{3H^2P_{,X}}{P_{,\phi}-24H^4\mathcal{G}'}\,d\phi. \tag{7}$$

In Equations (6) and (7) the subscripts hc and f refer to the horizon crossing of the physical scales and the end of the inflation, respectively.

By using the Arnowitt–Deser–Misner perturbed line element

$$\begin{aligned}ds^2=&-(1+2\mathcal{R})dt^2+2a(t)\mathcal{D}_i\,dt\,dx^i\\&+a^2(t)[(1-2\Phi)\delta_{ij}+2\Theta_{ij}]dx^idx^j,\end{aligned} \tag{8}$$

we present the cosmological linear perturbation in this setup. In the above perturbed metric, $\mathcal{D}^i$ is defined as $\mathcal{D}^i=\delta^{ij}\partial_j\mathcal{D}+v^i$ and the parameters $\mathcal{R}$ and $\mathcal{D}$ are 3-scalars. Also, v^i is a vector that satisfies the condition $v^i_{,i}=0$ (Mukhanov et al. 1992; Baumann 2009). In this metric, we have denoted the spatial symmetric and traceless shear 3-tensor by Θ_{ij} and the spatial curvature perturbation by Φ. To study the scalar perturbation at the linear level, we consider the scalar part of the perturbed metric within the uniform-field gauge (where $\delta\phi=0$) as

$$\begin{aligned}ds^2=&-(1+2\mathcal{R})dt^2+2a(t)\mathcal{D}_{,i}\,dt\,dx^i\\&+a^2(t)(1-2\Phi)\delta_{ij}dx^idx^j.\end{aligned} \tag{9}$$

By using this perturbed metric, action (2) is expanded up to the second order in perturbations, leading to the following quadratic action:

$$S_2=\int dt\,d^3x\,a^3\mathcal{W}_s\left[\dot{\Phi}^2-\frac{c_s^2}{a^2}(\partial\Phi)^2\right], \tag{10}$$

where

$$\begin{aligned}\mathcal{W}_s=&\left(\frac{1}{\kappa^2}-8H\dot{\mathcal{G}}\right)\\&\times\left[\left(\frac{1}{\kappa^2}-8H\dot{\mathcal{G}}\right)(3(XP_{,X}+2X^2P_{,XX})+144H^3\dot{\mathcal{G}})\right.\\&\left.+9\left(\frac{2H}{\kappa^2}-24H^2\dot{\mathcal{G}}\right)^2\right]\\&\times\left[3\left(\frac{2H}{\kappa^2}-24H^2\dot{\mathcal{G}}\right)^2\right]^{-1},\end{aligned} \tag{11}$$

and the square of the sound speed is given by

$$\begin{aligned}c_s^2=&3\left[2\left(\frac{1}{\kappa^2}-8H\dot{\mathcal{G}}\right)^2\left(\frac{2H}{\kappa^2}-24H^2\dot{\mathcal{G}}\right)H\right.\\&-\left(\frac{2H}{\kappa^2}-24H^2\dot{\mathcal{G}}\right)^2\left(\frac{1}{\kappa^2}-8\ddot{\mathcal{G}}\right)+4\left(\frac{1}{\kappa^2}-8H\dot{\mathcal{G}}\right)\\&\left(\frac{d}{dt}\left(\frac{1}{\kappa^2}-8H\dot{\mathcal{G}}\right)\right)\left(\frac{2H}{\kappa^2}-24H^2\dot{\mathcal{G}}\right)\\&\left.-2\left(\frac{1}{\kappa^2}-8H\dot{\mathcal{G}}\right)^2\left(\frac{d}{dt}\left(\frac{2H}{\kappa^2}-24H^2\dot{\mathcal{G}}\right)\right)\right]\left[\frac{1}{\kappa^2}-8H\dot{\mathcal{G}}\right]\\&\left[\left(\frac{1}{\kappa^2}-8H\dot{\mathcal{G}}\right)\left(3(XP_{,X}+2X^2P_{,XX})\right.\right.\\&\left.\left.-\frac{9}{\kappa^2}H^2+144H^3\dot{\mathcal{G}}\right)+9\left(\frac{2H}{\kappa^2}-24H^2\dot{\mathcal{G}}\right)^2\right].\end{aligned} \tag{12}$$

The following two-point correlation function is used to survey the power spectrum of the curvature perturbation:

$$\langle 0|\Phi(0,\boldsymbol{k}_1)\Phi(0,\boldsymbol{k}_2)|0\rangle = (2\pi)^3\delta^3(\boldsymbol{k}_1+\boldsymbol{k}_2)\frac{2\pi^2}{k^3}\mathcal{A}_s, \quad (13)$$

with $\mathcal{A}_s$, the power spectrum, defined by

$$\mathcal{A}_s = \frac{H^2}{8\pi^2\mathcal{W}_s c_s^3}. \quad (14)$$

The scalar spectral index is obtained by using the power spectrum as

$$n_s - 1 = \frac{d\ln\mathcal{A}_s}{d\ln k}|_{c_s k=aH}, \quad (15)$$

which is calculated at the time where the physical scales exit the sound horizon. In this setup the scalar spectral index is obtained as

$$n_s - 1 = -2\epsilon - \frac{\frac{d\left(\epsilon-\frac{4H\dot{\mathcal{G}}}{\kappa^{-2}}\right)}{dt}}{H\left(\epsilon-\frac{4H\dot{\mathcal{G}}}{\kappa^{-2}}\right)} - \frac{1}{Hc_s}\frac{d\,c_s}{dt}. \quad (16)$$

By focusing on the tensor part of the perturbed metric (8), we can explore the tensorial perturbations. In this regard, we write the 3-tensor Θ_{ij} as

$$\Theta_{ij} = \Theta_+\vartheta^+_{ij} + \Theta_\times\vartheta^\times_{ij}, \quad (17)$$

where $\vartheta^{(+,\times)}_{ij}$ are two polarization tensors that satisfy the reality and normalization conditions (De Felice & Tsujikawa 2011a, 2011b). Now, the quadratic (second-order) action for the tensor mode is the following expression:

$$S_T = \int dt\, d^3x\, a^3\mathcal{W}_T \times\left[\dot{\Theta}_+^2 - \frac{c_T^2}{a^2}(\partial\Theta_+)^2 + \dot{\Theta}_\times^2 - \frac{c_T^2}{a^2}(\partial\Theta_\times)^2\right]. \quad (18)$$

In this second-order action, the parameters $\mathcal{W}_T$ and c_T^2 are given by

$$\mathcal{W}_T = \frac{1}{4\kappa^2}\left(1 - 8\kappa^2H\dot{\mathcal{G}} + \frac{\kappa^2X\mathcal{N}}{M^2}\right), \quad (19)$$

$$c_T^2 = 1 + 8\kappa^2H\dot{\mathcal{G}} - \frac{2\kappa^2X\mathcal{N}}{M^2}. \quad (20)$$

For the tensor mode, the amplitude of the perturbations is defined as

$$\mathcal{A}_T = \frac{H^2}{2\pi^2\mathcal{W}_T c_T^3}, \quad (21)$$

and the tensor spectral index in this setup is given by

$$n_T = \frac{d\ln\mathcal{A}_T}{d\ln k} = 2\epsilon. \quad (22)$$

Another important perturbation parameter, the tensor-to-scalar ratio, is defined as the ratio of the amplitudes of the tensor mode versus the scalar mode:

$$r = \frac{\mathcal{A}_T}{\mathcal{A}_s} \simeq 16c_s\epsilon = -8c_s(n_T + 8\kappa^2H\dot{\mathcal{G}}). \quad (23)$$

For more details about obtaining the equations presented in this section, see De Felice & Tsujikawa (2011a, 2011b) and Nozari & Rashidi (2016b). By having the required equations, in the next sections we explore the observational viability of some GB models.

3. GB Inflation in a Model with the Canonical Scalar Field

In this section, we consider the case where

$$P(X,\phi) = X - V. \quad (24)$$

This choice of $P(X,\phi)$ corresponds to the simple inflation model, where the inflation rolls slowly down a nearly flat potential (Guth 1981; Albrecht & Steinhard 1982; Linde 1982). By this adoption, we have an inflation model in which a GB term is nonminimally coupled to the canonical scalar field. In this case, the scalar spectral index takes the following form:

$$n_s = 1 - \frac{16\chi\,V^3\mathcal{G}'' + 8\chi'V^3\mathcal{G}' + 3\chi\,V''\,V - 6\chi V'^2 + 3\chi'VV'}{V(8V^2\alpha' + 3V')}, \quad (25)$$

where

$$\chi = \frac{V'}{\kappa^2\,V} + \frac{8\kappa^2}{3}\mathcal{G}'\,V. \quad (26)$$

The tensor spectral index is given by

$$n_T = -2\left(\frac{1}{2\kappa^2}\frac{V'^2}{V^2} + \frac{4}{3}\kappa^2\mathcal{G}'\,V'\right). \quad (27)$$

Also, we have the following expression for the tensor-to-scalar ratio:

$$r = -8\left(-\frac{8}{3}\mathcal{G}'\,\chi\,V - \frac{\chi\,V'}{V}\right). \quad (28)$$

Note that in obtaining Equations (25)–(28) we have used the slow-roll conditions. Now, we have to choose some explicit functions for the potential and GB coupling function. After adopting the functions, we study the model numerically and compare the results with base[4] and base+GW[5] observational data sets.

3.1. Power-law Potential and Inverse Power-law GB Coupling

The model with the monomial potential and inverse monomial GB coupling function has been considered as the simplest primordial inflation model. In the absence of the GB effect, the simple inflation model with ϕ^2 and ϕ^4 potentials is not consistent with the base data (Akrami et al. 2018). We wonder whether the presence of the GB effect makes the model observationally viable. In this regard, we adopt the following potential and GB coupling function:

$$V = V_0\,\phi^n \quad \text{and} \quad \mathcal{G} = \mathcal{G}_0\,\phi^{-n}. \quad (29)$$

[4] Planck2018 TT, TE, EE+lowE+lensing+BAO +BK14.
[5] Planck2018 TT, TE, EE+lowE+lensing+BK14+ BAO+LIGO and Virgo2016.

By this choice, we find the following expressions for the perturbation parameters:

$$n_s = 1 - \frac{(n+2)(2\beta-1)n}{\phi^2}, \tag{30}$$

$$n_T = \frac{n^2(\beta-1)}{\phi^2}, \tag{31}$$

and

$$r = 8\,\frac{n^2(\beta-1)^2}{\phi^2}, \tag{32}$$

where

$$\beta = \frac{8}{3}V_0\,\mathcal{G}_0, \tag{33}$$

and we have set $\kappa^2 \equiv 1$. We can use Equation (7) to obtain the value of the scalar field at the time of the horizon crossing of the physical scales. Now, we perform a numerical analysis on the model's parameter space. In this regard, we explore r–n_s and r–n_t in confrontation with Planck2018 different data sets. To study the r–n_s behavior, we use the base data. Note that from this data set we have $n_s = 0.9658 \pm 0.0038$ and $r < 0.072$, based on the ΛCDM+r + $\frac{dn_s}{d\ln k}$ model. These constraints on the perturbation parameters imply the constraints $52.13 \leqslant N \leqslant 65.29$ and $0.407 \leqslant \mathcal{G} \leqslant 0.528$ on the GB model with $V = V_0\,\phi^n$ and $\mathcal{G} = \mathcal{G}_0\,\phi^{-n}$ and for $n = 2$. In the top panels of Figure 1, we see the r–n_s plane in the background of the base data. In plotting this figure (and all subsequent figures of this type), we have used $n = 2$, 4, $50 \leqslant N \leqslant 70$, and also $0 < \beta < 1$. As the figure shows, the r–n_s plane in the GB model with $n = 2$ in some ranges of the parameters space is consistent with the observational data. However, for $n = 4$, there is no consistency of the r–n_s plane with the base data.

In the sense that in studying the tensor spectral index we focus on the tensor part of the perturbations (the gravitational waves), we use the base+GW data to explore r–n_T. The results are shown in the bottom panels of Figure 1. In this case, the r–n_T plane for both $n = 2$ and $n = 4$ is consistent with the base +GW data. By numerical analysis of the model in this case, we have obtained some constraints on the model's parameter space, which are presented in Table 1. Note that Akrami et al. (2018) used the 68% CL on the measured parameter (n_s) and 95% CL for the upper bound on other parameters (r and n_T). In this respect, and given that we study these three parameters to obtain the constraints, both confidence levels are interesting to consider.

In summary, our numerical analysis shows that the GB inflation with $V = V_0\,\phi^n$ and $\mathcal{G} = \mathcal{G}_0\,\phi^{-n}$ for $n = 2$ is consistent with observational data if $\beta \sim \mathcal{O}(10^{-1})$. Also, this model with $V = V_0\,\phi^n$ and $\mathcal{G} = \mathcal{G}_0\,\phi^{-n}$ for $n = 4$ is ruled out. Note that, as can be seen from Table 1, any small variation of the parameter β can cause the model not to be consistent with the observational data. This means that, physically, not only the presence of the GB term but also the intensity of the coupling between the GB term (as the geometry side of the model) and the scalar field (as the energy-momentum side of the model) is very important in the viability of the model.

3.2. Power-law Potential and Dilaton-like GB Coupling

Inspired from heterotic string theory, the GB term appears to be coupled to the dynamical dilaton field with an exponential coupling function. This issue has been studied in Bamba et al. (2007). Therefore, in this subsection we adopt the following potential and GB coupling function:

$$V = V_0\,\phi^n \quad \text{and} \quad \mathcal{G} = \mathcal{G}_0\,e^{-\lambda\phi}. \tag{34}$$

In this case, we have the perturbation parameters of the model as

$$n_s = 1 - \frac{-n(n+2) + \beta\lambda\,e^{-\lambda\phi}\,\phi^{n+1}(2\lambda\phi - n)}{\phi^2}, \tag{35}$$

$$n_T = -\frac{n(n - \beta\lambda\,e^{-\lambda\phi}\,\phi^{n+1})}{\phi^2}, \tag{36}$$

and

$$r = \frac{8(n - \beta\lambda\,e^{-\lambda\phi}\,\phi^{n+1})^2}{\phi^2}. \tag{37}$$

Here we also use Equation (7) to obtain the value of the scalar field at the time of the horizon crossing of the physical scales and then study r–n_s and r–n_T behaviors. The top panels of Figure 2 show the r–n_s plane in the background of the base data for $N = 60$. As the figure shows, the r–n_s plane in the GB model with both $n = 2$ and $n = 4$ in some ranges of the parameters λ and β is consistent with the observational data.

In the bottom panels of Figure 2, we see the r–n_T plane in the background of the base+GW data. Considering that the scalar spectral index, the tensor spectral index, and the tensor-to-scalar ratio depend on both λ and β, to obtain the observational constraints, we fix λ in some sample values and obtain the observationally viable ranges of β. The results are shown in Table 2. In fact, according to our numerical analysis, the GB inflation with $V = V_0\,\phi^n$ and $\mathcal{G} = \mathcal{G}_0\,e^{-\lambda\phi}$ for $n = 2$ is consistent with observational data if $\beta \gtrsim \mathcal{O}(10^{-2})$. Also, this model for $n = 4$ is consistent with observational data if $\beta \sim \mathcal{O}(10^{-1})$.

4. GB Natural Inflation

In the inflation models, to fit with the cosmic microwave background anisotropy measurements, there should be a large number of e-folds of the scale factor. This means that the width of the potential in the inflation models must be much larger than its height. In this respect, the authors of Adams et al. (1991) have shown that, in order for the potential to be flat, the ratio between the height and the fourth power of the width must satisfy the constraint $\Delta V/(\Delta\phi)^4 \leqslant 10^{-6}$. In this constraint, Δ refers to the change in the corresponding parameters. In this regard, in 1990 Freese, Frieman, and Olinto proposed the natural inflation model (Freese et al. 1990). In their model, they have considered an axion-like particle (a pseudo-Nambu-Goldstone boson) as the field responsible for the primordial inflation. Invariance of the potential under a transformation of $\phi \to \phi$ + constant (a shift symmetry) ensures flatness of the potential (Freese et al. 1990; Freese & Kinney 2004). The symmetry is broken after enough inflation, and the inflation phase terminates. Based on these preliminaries, we consider a GB model where the potential is the natural potential type and

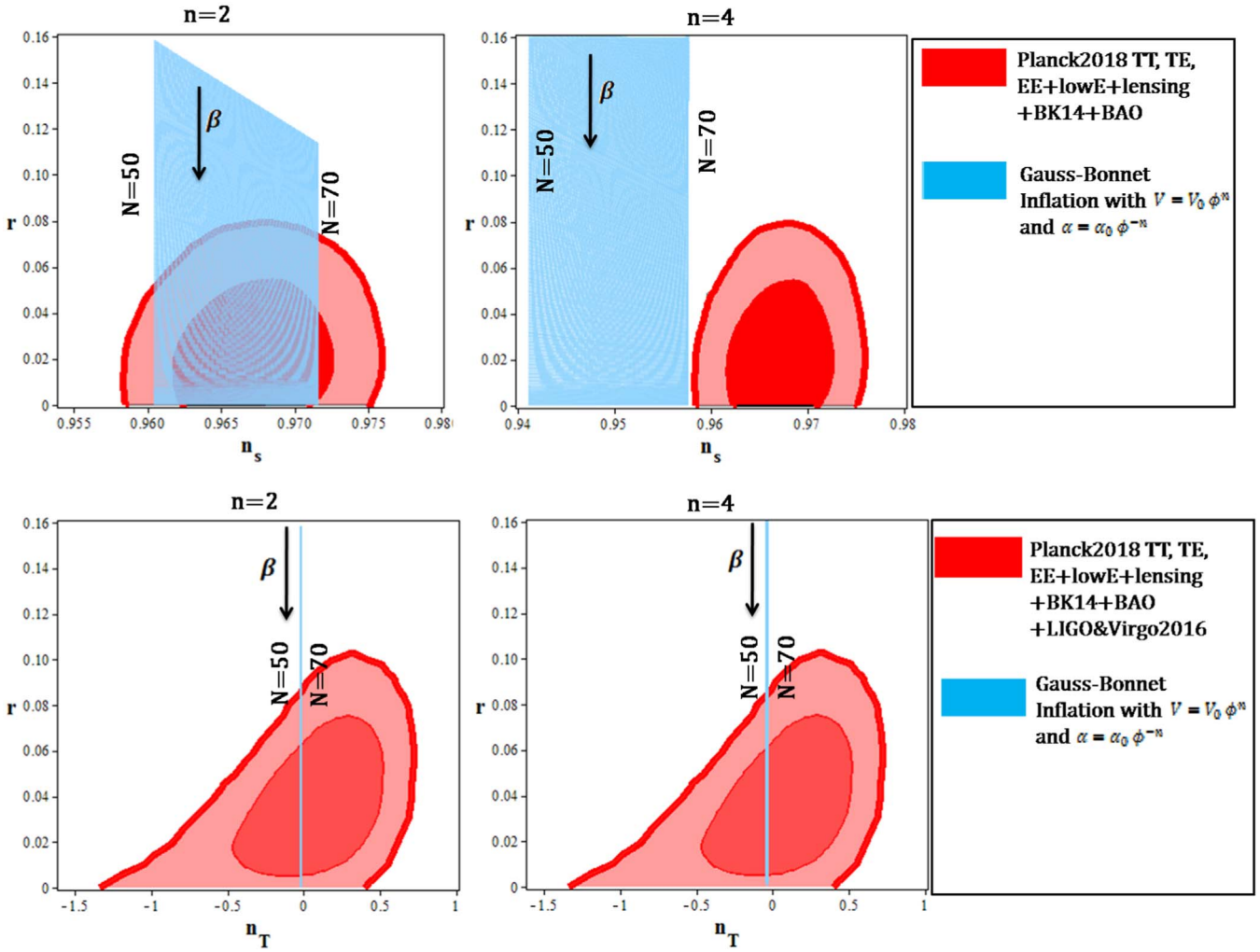

Figure 1. Tensor-to-scalar ratio vs. the scalar spectral index and tensor spectral index of the GB model with $V = V_0\,\phi^n$ and $\mathcal{G} = \mathcal{G}_0\,\phi^{-n}$.

Table 1
The Ranges of the Parameter β in Which the Tensor-to-Scalar Ratio, the Scalar Spectral Index, and the Tensor Spectral Index of the GB Model with $V = V_0\,\phi^n$ and $\mathcal{G} = \mathcal{G}_0\,\phi^{-n}$ are Consistent with Different Data Sets

		Planck2018 TT, TE, EE+lowE +lensing+BK14+BAO	Planck2018 TT, TE, EE+lowE +lensing+BK14+BAO	Planck2018 TT, TE, EE+lowE lensing+BK14+BAO +LIGO and Virgo2016	Planck2018 TT, TE, EE+lowE lensing+BK14+BAO LIGO and Virgo2016
	N	68% CL	95% CL	68% CL	95% CL
$n = 2$	50	Not consistent	$0.680 \leqslant \beta < 1$	$0.610 \leqslant \beta \leqslant 0.970$	$0.470 \leqslant \beta < 1$
	60	$0.601 \leqslant \beta < 1$	$0.410 \leqslant \beta < 1$	$0.520 \leqslant \beta \leqslant 0.964$	$0.340 \leqslant \beta < 1$
	70	$0.660 \leqslant \beta < 1$	$0.350 \leqslant \beta < 1$	$0.450 \leqslant \beta \leqslant 0.960$	$0.260 \leqslant \beta < 1$
$n = 4$	50	Not consistent	Not consistent	$0.810 \leqslant \beta \leqslant 0.985$	$0.730 \leqslant \beta < 1$
	60	Not consistent	Not consistent	$0.770 \leqslant \beta \leqslant 0.982$	$0.680 \leqslant \beta < 1$
	70	Not consistent	Not consistent	$0.730 \leqslant \beta \leqslant 0.980$	$0.630 \leqslant \beta < 1$

the GB coupling is the inverse of the natural potential as

$$V = V_0\left[1 + \cos\left(\frac{\phi}{f}\right)\right] \quad \text{and} \quad \mathcal{G} = \mathcal{G}_0\left[1 + \cos\left(\frac{\phi}{f}\right)\right]^{-1}. \tag{38}$$

Note that the natural inflation in its simplest realization has the above form of the potential. By these functions, the perturbation parameters take the following forms:

$$n_s = 1 - \frac{\left(\cos\left(\frac{\phi}{f}\right) - 3\right)(1-\beta)}{f^2\left(1 + \cos\left(\frac{\phi}{f}\right)\right)}, \tag{39}$$

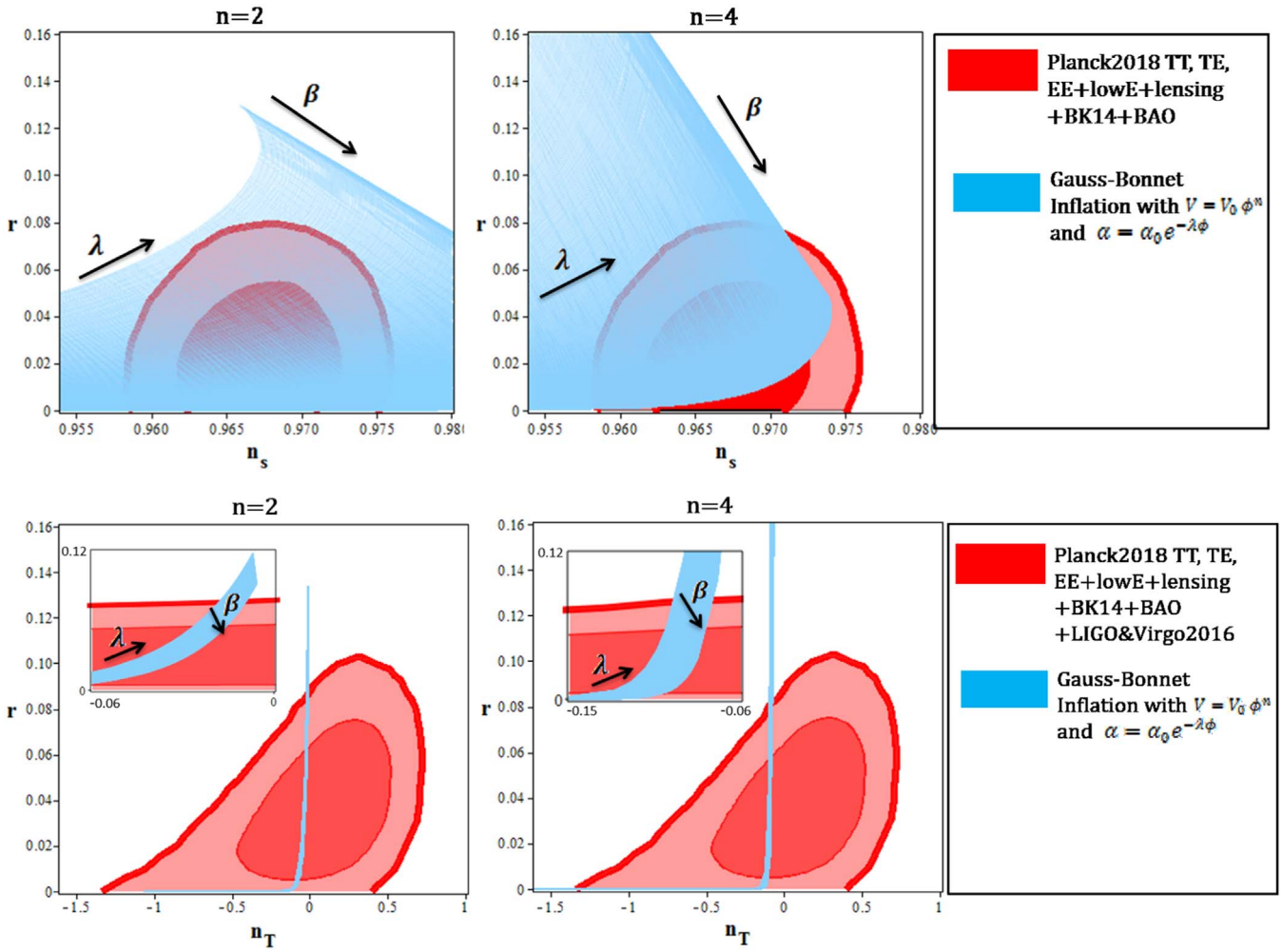

Figure 2. Tensor-to-scalar ratio vs. the scalar spectral index and tensor spectral index of the GB model with $V = V_0\,\phi^n$ and $\mathcal{G} = \mathcal{G}_0\,e^{-\lambda\phi}$.

Table 2
The Ranges of the Parameter β in Which the Tensor-To-Scalar Ratio, the Scalar Spectral Index, and the Tensor Spectral Index of the GB Model with $V = V_0\,\phi^n$ and $\mathcal{G} = \mathcal{G}_0\,e^{-\lambda\phi}$ are Consistent with Different Data Sets

		Planck2018 TT, TE, EE+lowE +lensing+BK14+BAO	Planck2018 TT,TE,EE+lowE +lensing+BK14+BAO	Planck2018 TT,TE,EE+lowE lensing+BK14+BAO +LIGO and Virgo2016	Planck2018 TT, TE, EE+lowE lensing+BK14+BAO LIGO and Virgo2016
	N	68% CL	95% CL	68% CL	95% CL
$n = 2$	10	$0.03 \leqslant \beta \leqslant 0.05$	$0.01 \leqslant \beta \leqslant 0.072$	$0.01 \leqslant \beta \leqslant 0.121$	$0.002 \leqslant \beta < 1$
	10^2	$0.062 \leqslant \beta \leqslant 0.084$	$0.016 \leqslant \beta \leqslant 0.095$	$0.031 \leqslant \beta \leqslant 0.184$	$0.020 \leqslant \beta < 1$
	10^4	$0.041 \leqslant \beta \leqslant 0.180$	$0.031 \leqslant \beta \leqslant 0.420$	$0.086 \leqslant \beta \leqslant 0.269$	$0.260 \leqslant \beta < 1$
$n = 4$	10	$0.610 \leqslant \beta \leqslant 0.683$	$0.580 \leqslant \beta \leqslant 0.716$	$0.435 \leqslant \beta \leqslant 0.812$	$0.016 \leqslant \beta \leqslant 0.871$
	10^2	$0.642 \leqslant \beta \leqslant 0.711$	$0.621 \leqslant \beta \leqslant 0.743$	$0.483 \leqslant \beta \leqslant 0.865$	$0.033 \leqslant \beta \leqslant 0.895$
	10^4	$0.693 \leqslant \beta \leqslant 0.789$	$0.670 \leqslant \beta \leqslant 0.826$	$0.506 \leqslant \beta \leqslant 0.884$	$0.081 \leqslant \beta \leqslant 0.910$

$$n_T = -\frac{(-1+\beta)\left(\cos\left(\frac{\phi}{f}\right)-1\right)}{f^2\left(1+\cos\left(\frac{\phi}{f}\right)\right)}, \tag{40}$$

$$r = \frac{8(-1+\beta)^2\left(1-\cos\left(\frac{\phi}{f}\right)\right)}{f^2\left(1+\cos\left(\frac{\phi}{f}\right)\right)}. \tag{41}$$

By using Equation (7), to obtain the value of the scalar field at horizon crossing, and Equations (39)–(41), we can study the model numerically. To this end, we adopt $N = 60$ and explore r–n_s and r–n_T planes for various values of f and β. The top panel of Figure 3 shows the tensor-to-scalar ratio versus the scalar spectral index in the background of the base data. As Figure 3 shows, the natural GB inflation in some ranges of the parameter space is observationally viable.

Tensor-to-scalar ratio versus the tensor spectral index in the background of the base+GW data is shown in the bottom panel

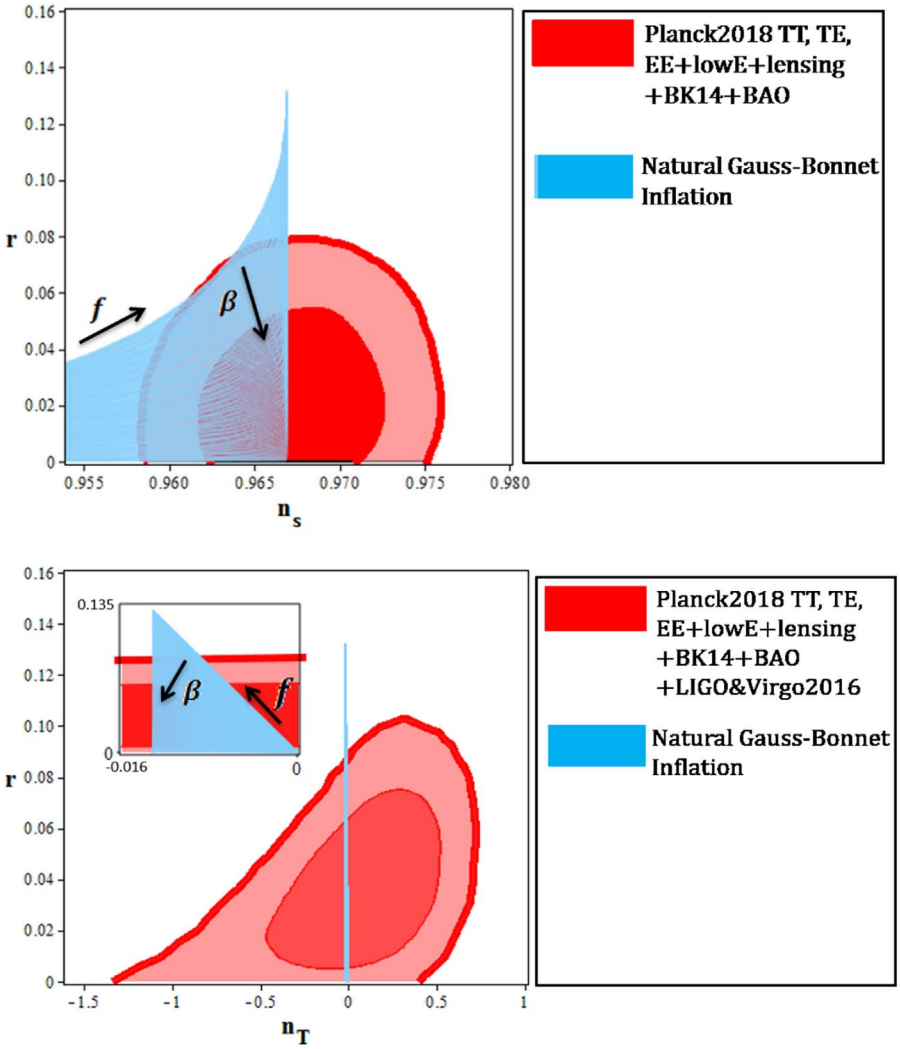

Figure 3. Tensor-to-scalar ratio vs. the scalar spectral index and tensor spectral index of the GB natural inflation.

Table 3
The Ranges of the Parameter β in Which the Tensor-To-Scalar Ratio, the Scalar Spectral Index, and the Tensor Spectral Index of the GB Natural Inflation Are Consistent with Different Data Sets

	Planck2018 TT, TE, EE+lowE +lensing+BK14+BAO	Planck2018 TT, TE, EE+lowE +lensing+BK14+BAO	Planck2018 TT, TE, EE+lowE lensing+BK14+BAO +LIGO and Virgo2016	Planck2018 TT, TE, EE+lowE lensing+BK14+BAO LIGO and Virgo2016
N	68% CL	95% CL	68% CL	95% CL
4	$0.635 \leqslant \beta < 1$	$0.525 \leqslant \beta < 1$	$0 \leqslant \beta \leqslant 0.962$	All values of β
15	$0.578 \leqslant \beta < 1$	$0.345 \leqslant \beta < 1$	$0.520 \leqslant \beta \leqslant 0.962$	$0.341 \leqslant \beta < 1$
35	$0.596 \leqslant \beta < 1$	$0.393 \leqslant \beta < 1$	$0.520 \leqslant \beta \leqslant 0.962$	$0.341 \leqslant \beta < 1$
60	$0.597 \leqslant \beta < 1$	$0.400 \leqslant \beta < 1$	$0.524 \leqslant \beta \leqslant 0.962$	$0.346 \leqslant \beta < 1$

of Figure 3. By performing a numerical analysis, we have found some constraints on the model's parameters, which have been summarized in Table 3. Note that the natural inflation with $N = 50$ is not consistent with new observational data. However, when we consider the GB effect, this model for $\beta \geqslant 0.65$ is consistent with base and base+GW data sets.

5. GB α-attractor

In recent years, the idea of the "cosmological attractor" has attracted the attention of some cosmologists. Among the models that incorporate the idea of cosmological attractors, we mention the conformal attractor (Kallosh & Linde 2013a, 2013b) and α-attractor models (Ferrara et al. 2013; Kallosh et al. 2013, 2014a). The important characteristic property in the conformal attractor model is that, in the case of large e-folds number, it has the universal prediction for the primordial curvature perturbations and the tensor-to-scalar ratio as $n_s = 1 - \frac{2}{N}$ and $r = \frac{12}{N^2}$. Considering the single-field α-attractor model, the universal predictions for the mentioned parameters are $n_s = 1 - \frac{2}{N}$ and $r = \frac{12\alpha}{N^2}$. In this section, we consider the GB effect on the α-attractor model. We consider both potentials leading to the α-attractor: E-model

and T-model. We also adopt the E-model and T-model GB coupling function and study the inflation in this setup.

5.1. E-model

In Kallosh & Linde (2013b), the authors have considered a model with two real scalar fields, φ and ψ, which are nonminimally coupled to the gravity. They have also considered a potential term as $V\left(\varphi, \psi\right) = \frac{\lambda}{4}\varphi^2(\varphi - \psi)^2$ by which the SO(1, 1) symmetry has been broken. By using the conformal gauge as $\psi^2 - \varphi^2 = 6$ and introducing a canonically normalized field as $\varphi = \sqrt{6}\cosh\frac{\phi}{\sqrt{6}}$ and $\psi = \sqrt{6}\sinh\frac{\phi}{\sqrt{6}}$, they have obtained an exponential-type potential named E-model, which we use in this subsection. In this case, we consider the following potential and GB coupling:

$$V = V_0\left[1 - \exp\left(-\sqrt{\frac{2\kappa^2}{3\alpha}}\,\phi\right)\right]^{2n}$$
$$\text{and} \quad \mathcal{G} = \mathcal{G}_0\left[1 - \exp\left(-\sqrt{\frac{2\kappa^2}{3\alpha}}\,\phi\right)\right]^{2n}, \tag{42}$$

where the potential V is an E-model potential. With these functions, we obtain the perturbation parameters from Equations (25)–(28). In this case, the scalar spectral index takes the following form:

$$n_s = 1 - \frac{8}{9}\frac{nZ(256\,\beta^2\,Y^{8\,n}Zn\kappa^4 - 96\,\beta^2\,Y^{8\,n}\,\kappa^4 + 24\,\kappa^4\beta\,Y^{4\,n}\,nZ - 24\,\kappa^4\beta\,Y^{4\,n})}{Y^2\alpha(8\,\beta\,Y^{4\,n} + 3)}$$
$$- \frac{8}{9}\frac{nZ(48\,\beta\,Y^{4\,n}\,Zn - 36\,\beta\,Y^{4\,n} - 9\,nZ - 9)}{Y^2\alpha(8\,\beta\,Y^{4\,n} + 3)}. \tag{43}$$

The tensor spectral index in the E-model GB inflation is given by

$$n_T = -\frac{8}{9}\frac{n^2Z^2(8\,\kappa^4\beta\,Y^{4\,n} + 3)}{\alpha\,Y^2}. \tag{44}$$

Also, we obtain the following expression for the tensor-to-scalar ratio in this case:

$$r = \frac{64}{27}\frac{n^2Z^2(64\,\kappa^4\beta^2\,Y^{8\,n} + 24\,\kappa^4\beta\,Y^{4\,n} + 24\,\beta\,Y^{4\,n} + 9)}{\alpha\,Y^2}. \tag{45}$$

In these equations, we have defined the following parameters:

$$Y = 1 - Z \quad \textit{and} \quad Z = e^{-\frac{\sqrt{6}}{3}\sqrt{\frac{\kappa^2}{\alpha}}\,\phi}. \tag{46}$$

5.2. T-model

Another interesting case in the α-attractor model is T-model potential. Kallosh & Linde (2013a) have studied a model with two nonminimally coupled scalar fields and the potential term as $V\left(\varphi, \psi\right) = \frac{1}{36}F(\varphi/\psi)(\varphi^2 - \psi^2)^2$, which breaks the SO(1, 1) symmetry. Note that $F(\varphi/\psi)$ is an arbitrary function. By using the gauge and canonically normalized field used in obtaining the E-model potential, they have found the potential as $V(\phi) = F(\tanh(\phi/\sqrt{6}))$. In the case of the simplest set of functions as $F(\varphi/\psi) = \lambda(\varphi/\psi)^{2n}$, the T-model potential has been obtained. Now, in this subsection, we consider the case where the potential and GB coupling function are T-model type, as

$$V = V_0\tanh^{2n}\left(\sqrt{\frac{\kappa^2}{6\alpha}}\,\phi\right),$$
$$\mathcal{G} = \mathcal{G}_0\tanh^{2n}\left(\sqrt{\frac{\kappa^2}{6\alpha}}\,\phi\right). \tag{47}$$

By substituting the potential and GB coupling function into Equations (25)–(28), we obtain the scalar spectral index as

$$n_s = 1 + \frac{2}{9}\frac{n(192\,\beta^2\,\mathcal{U}^{8n}\kappa^4\mathcal{V} - 256\beta^2\,\mathcal{U}^{8n}\,n\kappa^4 - 96\,\beta\,\mathcal{U}^{8n}\kappa^4 + 48\,\kappa^4\beta\,\mathcal{U}^{4n}\mathcal{V} + 9\,n - 9)}{\mathcal{V}(\mathcal{V} - 1)(8\,\beta\,\mathcal{U}^{4n} + 3)\alpha}$$
$$+ \frac{2}{9}\frac{n(-24\kappa^4\beta\,\mathcal{U}^{4n}\,n - 24\kappa^4\beta\,\mathcal{U}^{4n} + 72\beta\,\mathcal{U}^{4n}\,\mathcal{V} - 48\beta\,\mathcal{U}^{4n}\,n - 36\beta\,\mathcal{U}^{4n} + 18\mathcal{V})}{\mathcal{V}(\mathcal{V} - 1)(8\,\beta\,\mathcal{U}^{4n} + 3)\alpha}, \tag{48}$$

the tensor spectral index as

$$n_T = -\frac{2}{9}\frac{n^2(8\,\kappa^4\beta\,\mathcal{U}^{4n} + 3)}{\alpha\,\mathcal{V}(\mathcal{V} - 1)}, \tag{49}$$

and finally the tensor-to-scalar ratio as

$$r = \frac{16}{27}\frac{n^2(64\kappa^4\beta^2\,\mathcal{U}^{8n} + 24\,\kappa^4\beta\,\mathcal{U}^{4n} + 24\beta\,\mathcal{U}^{4n} + 9)}{\mathcal{V}(\mathcal{V} - 1)\alpha}, \tag{50}$$

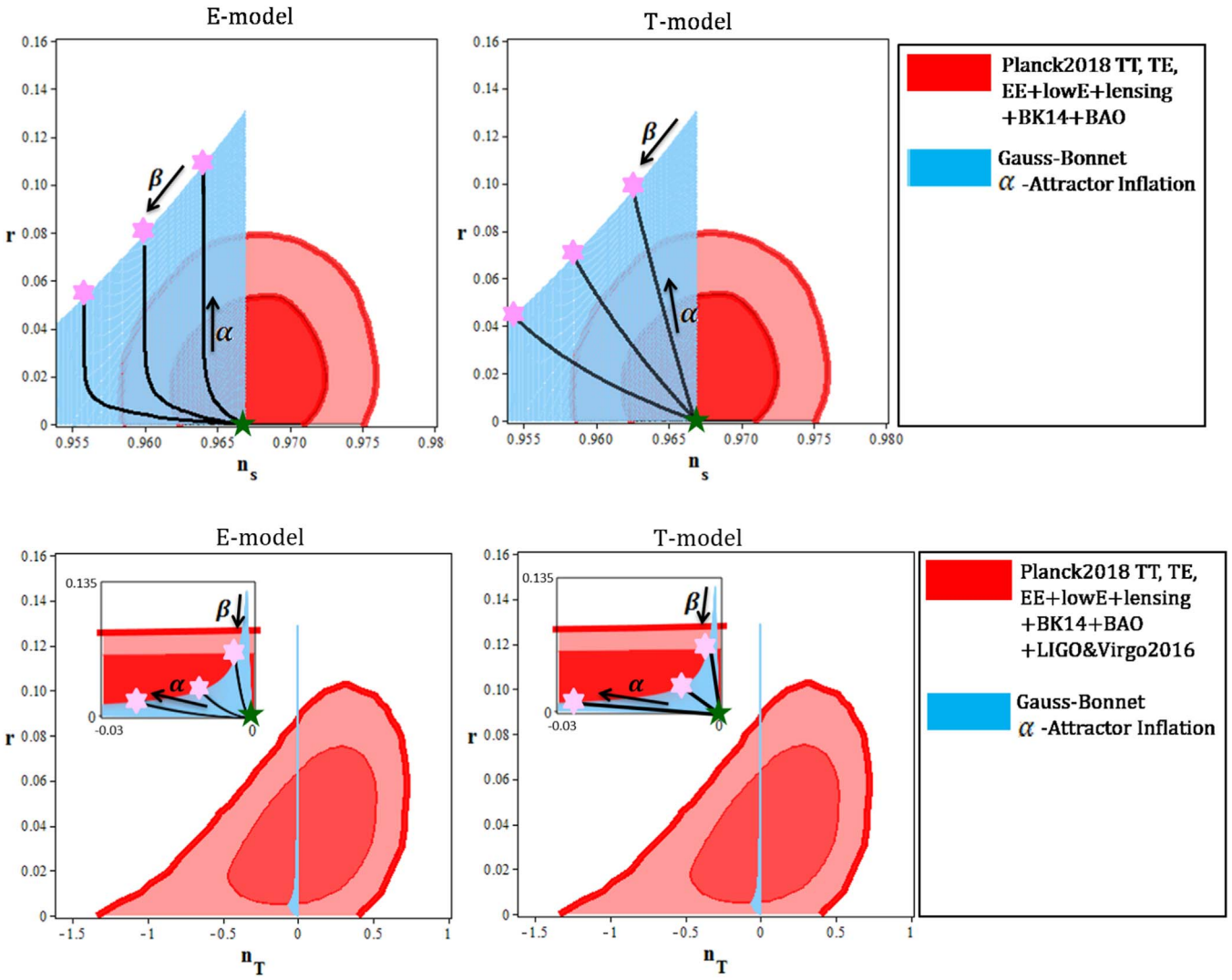

Figure 4. Tensor-to-scalar ratio vs. the scalar spectral index and tensor spectral index of the GB α-attractor. The left panels correspond to the case where both the potential and GB coupling are E-model. The right panels correspond to the case where both the potential and GB coupling are T-model. The black lines have been plotted to show that the GB α-attractor model in the small-α limit reaches an attractor (green star) and in the large-α limit meets the GB model with the ϕ^2 potential and GB coupling (pink stars).

where the parameters $\mathcal{U}$ and $\mathcal{V}$ are given by

$$\mathcal{U} = \tanh\left(\sqrt{\frac{\kappa^2}{6\alpha}}\,\phi\right) \tag{51}$$

and

$$\mathcal{V} = \cosh^2\left(\sqrt{\frac{\kappa^2}{6\alpha}}\,\phi\right). \tag{52}$$

By substituting the value of the scalar field at horizon crossing in Equations (43)–(45) and Equations (48)–(50), we can study the GB α-attractor model numerically. The results are shown in Figures 7 and 8. The α-attractor models with E-model and T-model potential meet the model with ϕ^n potential in the $\alpha \to \infty$ limit. On the other hand, these models in $\alpha \to 0$ and large-N limits reach an attractor point characterized by the following scalar spectral index and tensor-to-scalar ratio:

$$n_s = 1 - \frac{2}{N}, \quad r = \frac{12\alpha}{N^2}. \tag{53}$$

The top panels of Figure 4 show the tensor-to-scalar ratio versus the scalar spectral index of a GB model in the background of the base data, for E-model potential and coupling function (left panel) and T-model potential and coupling function (right panel). The black lines have been plotted to show that the GB α-attractor model in the small α limit reaches an attractor (green star) and in the large α limit meets the GB model with ϕ^2 potential and GB coupling (pink stars). This figure has been plotted with $n = 2$ and $N = 60$. As we see from the figure, the GB model with the ϕ^2 potential and GB coupling function is not consistent with the base data. However, when we consider the E-model or T-model potential and GB coupling function, it is possible to find some ranges in the parameter space leading to observationally viable values of r and n_s. Our analysis on r–n_s viability shows that E-model GB inflation is consistent with base data 68% CL if $\alpha < 78$ and at

Table 4
The Ranges of the Parameter β in Which the Tensor-To-Scalar Ratio, the Scalar Spectral Index, and the Tensor Spectral Index of the GB α-Attractor Model with $n = 2$ and $N = 60$ are Consistent with Different Data Sets

		Planck2018 TT, TE, EE+lowE +lensing+BK14+BAO	Planck2018 TT, TE, EE+lowE +lensing+BK14+BAO	Planck2018 TT, TE, EE+lowE lensing+BK14+BAO +LIGO and Virgo2016	Planck2018 TT, TE, EE+lowE lensing+BK14+BAO LIGO and Virgo2016
	N	68% CL	95% CL	68% CL	95% CL
E-model	20	$\beta \leqslant 5.17 \times 10^{-2}$	$\beta \leqslant 5.31 \times 10^{-2}$	$\beta < 3.10 \times 10^{-3}$	All values of β
	50	$\beta \leqslant 4.92 \times 10^{-2}$	$\beta \leqslant 5.04 \times 10^{-2}$	$\beta < 4.52 \times 10^{-3}$	All values of β
	80	$3.23 \times 10^{-4} \leqslant \beta \leqslant 4.56 \times 10^{-2}$	$\beta \leqslant 4.81 \times 10^{-2}$	$\beta < 8.22 \times 10^{-3}$	All values of β
T-model	20	$\beta \leqslant 3.30 \times 10^{-1}$	$\beta \leqslant 4.01 \times 10^{-1}$	$\beta < 8.11 \times 10^{-3}$	All values of β
	50	$3.03 \times 10^{-4} \leqslant \beta \leqslant 1.42 \times 10^{-1}$	$\beta \leqslant 9.03 \times 10^{-2}$	$\beta < 9.82 \times 10^{-3}$	All values of β
	80	$4.28 \times 10^{-4} \leqslant \beta \leqslant 1.14 \times 10^{-1}$	$\beta \leqslant 7.01 \times 10^{-2}$	$2.37 \times 10^{-4} < \beta < 1.43 \times 10^{-2}$	All values of β

95% CL if $\alpha < 4.1 \times 10^2$. Also, T-model GB inflation has consistency with base data at 68% CL if $\alpha < 43$ and at 95% CL if $\alpha < 91$.

The bottom panels of Figure 4 show the tensor-to-scalar ratio versus the tensor spectral index in the background of base +GW data. By performing a numerical analysis on r–n_T viability, we find that E-model GB inflation is consistent with base+GW data at 68% CL if $2.12 < \alpha < 1.6 \times 10^2$ and at 95% CL if $\alpha < 7.4 \times 10^2$. Also, in T-model GB inflation we find the constraints $2.43 < \alpha < 73$ at 68% CL and $\alpha < 2 \times 10^2$ at 95% CL. However, the values of α imply some constraints on the GB coupling parameter, which have been summarized in Table 4, for some sample values of α.

By these considerations, we conclude that the GB inflation with both E-model and T-model potentials and GB coupling functions is consistent with the observational data if $\beta \lesssim \mathcal{O}(10^{-3})$.

6. GB Inflation in a Model with the Tachyon Field

The tachyon field is a scalar field associated with D-branes in string theory (Sen 1999, 2002a, 2002b). This field, which is described by the DBI action, has interesting cosmological applications. The early-time inflation in the history of the universe might be caused by a slow-rolling tachyon field (Feinstein 2002; Sami et al. 2002; Nozari & Rashidi 2014). Also, it is possible that the current acceleration phase of the universe is due to the presence of the tachyon field as the dark energy component (Padmanabhan 2002; Gorini et al. 2004; Copeland et al. 2005). These features make the tachyon field cosmologically interesting. In the case of the tachyon field, $P(X, \phi)$ is given by the following expression:

$$P(X, \phi) = -V\sqrt{1 - 2X}. \tag{54}$$

Now, the scalar spectral index takes the following form:

$$n_s = 1 - \frac{16\chi\, V^3\mathcal{G}'' + 8\chi' V^3\mathcal{G}' + 3\chi\, V''\, V - 6\chi V'^2 + 3\chi' VV'}{V(8V^2\alpha' + 3V')} \tag{55}$$

The tensor spectral index is given by

$$n_T = -2\left(\frac{1}{2\kappa^2}\frac{V'^2}{V^2} + \frac{4}{3}\kappa^2\mathcal{G}'\, V'\right), \tag{56}$$

and we have the following expression for the tensor-to-scalar ratio:

$$r = -8\left(-\frac{8}{3}\mathcal{G}'\,\chi\, V - \frac{\chi\, V'}{V}\right). \tag{57}$$

In Equations (55)–(57), the parameter χ is given by

$$\chi = \frac{V'}{\kappa^2\, V^2} + \frac{8\kappa^2}{3}\,\mathcal{G}'. \tag{58}$$

Now, by choosing some explicit functions for the potential and GB coupling, we study this model numerically.

6.1. Power-law Potential and Inverse Power-law GB Coupling

Our first choices for the tachyon GB model are the following potential and GB coupling function:

$$V = V_0\,\phi^n \quad \text{and} \quad \mathcal{G} = \mathcal{G}_0\,\phi^{-n}. \tag{59}$$

By these adoptions, we find

$$n_s = 1 - 2\,\frac{(2\,n\beta\,\kappa^4 + 2\,\beta\,\kappa^4 - n - 1)n}{\phi^{n+2}}, \tag{60}$$

$$n_T = -\phi^{-2-n}n^2(1 - 2\,\beta), \tag{61}$$

and

$$r = 8[\phi^{-2-n}n^2(2\,\beta - 1)^2]. \tag{62}$$

To compare the model with observational data, we substitute the value of the scalar field at the time of the horizon crossing of the physical scales in the above equations. Then, we perform the numerical analysis on the parameters. In the top panels of Figure 5, we see the r–n_s plane in the background of the base data for $50 \leqslant N \leqslant 70$. As the figure shows, including the GB effect makes the tachyon model more observationally viable. Our numerical analysis shows that r–n_s in the tachyon GB inflation with $V = V_0\,\phi^n$ and $\mathcal{G} = \mathcal{G}_0\,\phi^{-n}$ is consistent with 68% CL of the base data if $N < 54.2$ for $n = 2$ and $N < 60.5$ for $n = 4$. In this case, r–n_s is consistent with 95% CL of base data if $N < 62.4$ for $n = 2$ and $N < 70$ for $n = 4$.

The bottom panels of Figure 5 show the tensor-to-scalar ratio versus the tensor spectral index of the tachyon GB model with $V = V_0\,\phi^n$ and $\mathcal{G} = \mathcal{G}_0\,\phi^{-n}$. The tachyon GB model is consistent with observational data in some ranges of β. In Table 5, we present the constraints on β for $N = 50, 60, 70$ and $n = 2, 4$, which makes the model observationally viable. In this regard, we find that the tachyon GB inflation with $V = V_0\,\phi^n$

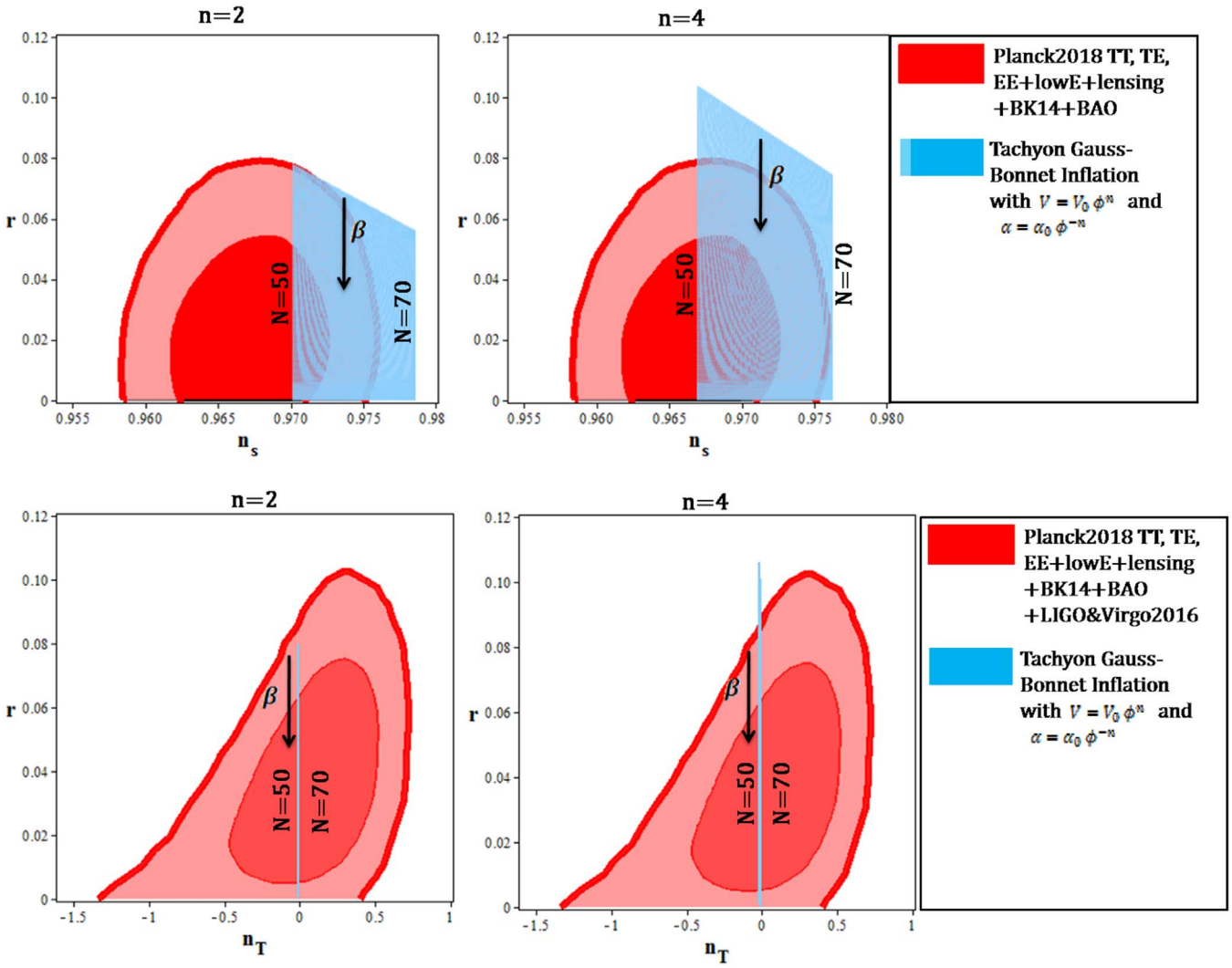

Figure 5. Tensor-to-scalar ratio vs. the scalar spectral index and tensor spectral index of the tachyon GB model with $V = V_0\,\phi^n$ and $\mathcal{G} = \mathcal{G}_0\,\phi^{-n}$.

and $\mathcal{G} = \mathcal{G}_0\,\phi^{-n}$ for $n = 2$ and $n = 4$ is consistent with observational data if $\beta \sim \mathcal{O}(10^{-1})$.

6.2. Power-law Potential and Dilaton-like GB Coupling

In this subsection, we consider the following potential and GB coupling:

$$V = V_0\,\phi^n \quad \text{and} \quad \mathcal{G} = \mathcal{G}_0\,e^{-\lambda\phi}. \tag{63}$$

Now, we have

$$n_s = 1 - \frac{-e^{\lambda\,\phi}\chi\,n^2 + \beta\,\lambda^2\chi\,\phi^{n+2} - \beta\,\lambda\,\phi^{n+2}\chi' + e^{\lambda\,\phi}n\chi'\,\phi - e^{\lambda\,\phi}\chi\,n}{\phi(\phi^{n+1}\beta\,\lambda - ne^{\lambda\,\phi})}, \tag{64}$$

$$n_T = -\frac{(-\kappa^4\beta\,\lambda\,e^{-\lambda\,\phi} + n\phi^{-n-1})n}{\phi}, \tag{65}$$

and

$$r = 8\,\frac{-e^{-2\,\lambda\,\phi}\phi^{n+1}\beta^2\lambda^2 + 2\,e^{-\lambda\,\phi}n\beta\,\lambda - \phi^{-n-1}n^2}{\phi}. \tag{66}$$

By using these perturbation parameters, we perform a numerical analysis on the model. The top panels of Figure 6 show the behavior of r–n_s of the tachyon GB model with functions given by Equation (63), in the background of the base data for $N = 60$. Our numerical analysis shows that, in this case, the tachyon GB model with $0.15 < \lambda$ (for $n = 2$) and $0.10 < \lambda$ (for $n = 4$) is consistent with the base data at 95% CL. Also, this model with $0.19 < \lambda < 0.37$ (for $n = 2$) and $0.18 < \lambda < 0.52$ (for $n = 4$) is consistent with the base data at 68% CL.

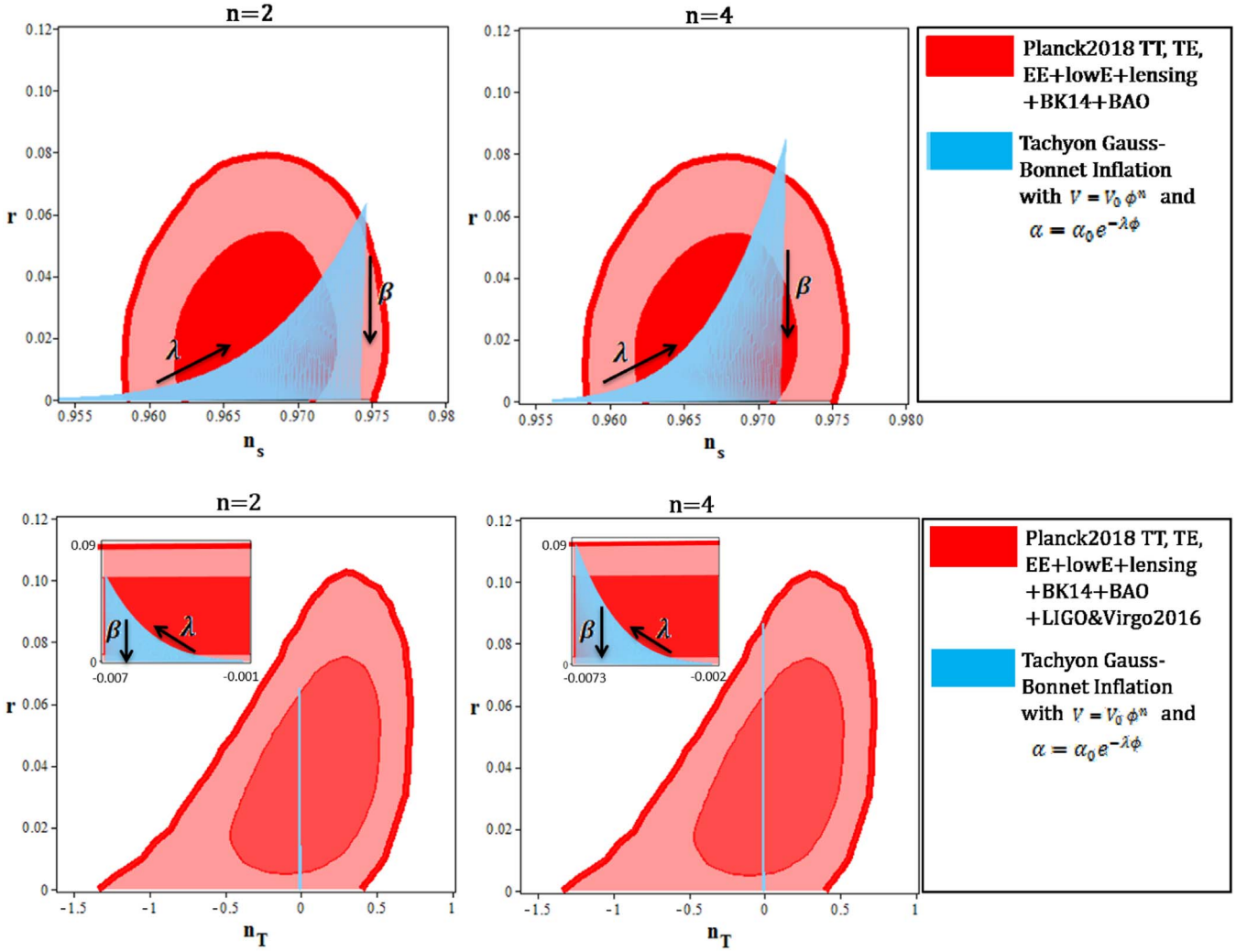

Figure 6. Tensor-to-scalar ratio vs. the scalar spectral index and tensor spectral index of the tachyon GB model with $V = V_0\,\phi^n$ and $\mathcal{G} = \mathcal{G}_0\,e^{-\lambda\phi}$.

Table 5
The Ranges of the Parameter β in Which the Tensor-To-Scalar Ratio, the Scalar Spectral Index, and the Tensor Spectral Index of the Tachyon GB Model with $V = V_0\,\phi^n$ and $\mathcal{G} = \mathcal{G}_0\,\phi^{-n}$ Are Consistent with Different Data Sets

		Planck2018 TT, TE, EE+lowE +lensing+BK14+BAO	Planck2018 TT, TE, EE+lowE +lensing+BK14+BAO	Planck2018 TT, TE, EE+lowE lensing+BK14+BAO +LIGO and Virgo2016	Planck2018 TT, TE, EE+lowE lensing+BK14+BAO LIGO and Virgo2016
	N	68% CL	95% CL	68% CL	95% CL
$n = 2$	50	$0.360 \leqslant \beta < 1$	All values	$0.201 \leqslant \beta \leqslant 0.938$	All values
	60	Not consistent	$0.251 \leqslant \beta < 1$	$0.042 \leqslant \beta \leqslant 0.924$	All values
	70	Not consistent	Not consistent	$\beta \leqslant 0.911$	All values
$n = 4$	50	$0.498 \leqslant \beta < 1$	$0.254 \leqslant \beta < 1$	$0.403 \leqslant \beta \leqslant 0.953$	$0.188 \leqslant \beta < 1$
	60	$0.685 \leqslant \beta < 0.892$	$0.205 \leqslant \beta < 1$	$0.283 \leqslant \beta \leqslant 0.943$	$0.020 \leqslant \beta < 1$
	70	Not consistent	Not consistent	$0.164 \leqslant \beta \leqslant 0.937$	All values

The tensor spectral index versus the tensor-to-scalar ratio of the tachyon GB model with $V = V_0\,\phi^n$ and $\mathcal{G} = \mathcal{G}_0\,e^{-\lambda\phi}$, in the background of the base+GW data, is shown in the bottom panels of Figure 6. As the figure shows, for all values of λ and β, the tensor-to-scalar ratio and the tensor spectral index of this model are consistent with base+GW data at 95% CL. However, there are some constraints on λ and β at 68% CL. At this level, the constraints on λ are $0.23 < \lambda$ (for $n = 2$) and $0.19 < \lambda$ (for $n = 4$). For some sample values of λ, the constraints on β are summarized in Table 6. According to this analysis, for the tachyon GB inflation with $V = V_0\,\phi^n$ and $\mathcal{G} = \mathcal{G}_0\,e^{-\lambda\phi}$ and for $n = 2$, we cannot find any constraint on β. This is because this model for all values of β is consistent with observational data at 95% CL. For $n = 4$, if we assume large values of λ as $\lambda \sim \mathcal{O}(10^4)$, we find that the constraint $\beta \lesssim \mathcal{O}(10^{-2})$.

7. DBI GB Inflation

There is another proposal arisen from string theory, which is based on the DBI action (Alishahiha et al. 2004; Silverstein & Tong 2004). This proposal suggests that the field responsible for inflation is characterized by the radial coordinate of a D3 brane that moves in a "throat" (often AdS_5 throat) region of a warped compactified space. Both the speed of the brane and the warp factor of the throat set a speed limit on the brane's motion. In this model, besides the potential, there is a function of the scalar field related to the local geometry of the compact manifold traversed by the D3 brane. Also, the kinetic term of the field is noncanonical (Silverstein & Tong 2004).

In the DBI model, we have

$$P(X,\phi) = -\mathcal{F}^{-1}(\phi)\sqrt{1-2\mathcal{F}(\phi)X} - V(\phi), \tag{67}$$

By this definition, the scalar spectral index takes the following forms:

$$\begin{aligned} n_s = 1 &- 2M\chi - \left[4M\chi^2(\mathcal{F}^{-1}+V)\left(\frac{B}{M}+\frac{\chi'}{\chi}\right)\right. \\ &- \frac{16}{3}\alpha'\chi^2(\mathcal{F}^{-1}+V)^3 \\ &\left.\times\left(\frac{\alpha''}{\alpha'}+2\,\frac{-\frac{\mathcal{F}'}{\mathcal{F}^2}+V'}{\mathcal{F}^{-1}+V}+\frac{\chi'}{\chi}\right)\right] \\ &\times\left[2M\chi-\frac{8}{3}\alpha'\chi(\mathcal{F}^{-1}+V)^2\right]^{-1}. \end{aligned} \tag{68}$$

The tensor spectral index in the DBI GB model is given by

$$n_T = -2M\chi, \tag{69}$$

and the tensor-to-scalar ratio is obtained as follows:

$$r = -16\,M\,\chi + \frac{64}{3}\alpha'\chi(V+\mathcal{F}^{-1})^2, \tag{70}$$

where

$$\chi = \frac{1}{2}\,\frac{\frac{\mathcal{F}'}{\mathcal{F}^2}-V'-24\,H^4\alpha'}{\kappa^2(\mathcal{F}^{-1}+V)^2}, \tag{71}$$

$$M = \frac{\mathcal{F}'}{\mathcal{F}^2} - 4\,\frac{\mathcal{F}'(\mathcal{F}^{-1}+V)^4\chi^2}{\mathcal{F}} - V', \tag{72}$$

and

$$\begin{aligned} B = \frac{\mathcal{F}''}{\mathcal{F}^2} &- 2\,\frac{\mathcal{F}'^2}{\mathcal{F}^3} - 4\,\frac{(\mathcal{F}''\mathcal{F}-\mathcal{F}'^2)(\mathcal{F}^{-1}+V)^4\chi^2}{\mathcal{F}^2} \\ &- 4\,\frac{\mathcal{F}'\left(-4\,\frac{\mathcal{F}'}{\mathcal{F}^2}+4\,V'\right)(\mathcal{F}^{-1}+V)^3\chi^2}{\mathcal{F}} \\ &- 8\,\frac{\mathcal{F}'(\mathcal{F}^{-1}+V)^4\chi\chi'}{\mathcal{F}} - V''. \end{aligned} \tag{73}$$

As in previous sections, by choosing some explicit functions for the potential and coupling function, we study this model numerically.

7.1. Power-law Potential and Inverse Power-law GB Coupling

We start this subsection by adopting the following potential and GB coupling function:

$$V = V_0\,\phi^n, \quad \mathcal{F} = \mathcal{F}_0\phi^{-n} \quad \text{and} \quad \mathcal{G} = \mathcal{G}_0\,\phi^{-n}. \tag{74}$$

In this case, we get

$$\begin{aligned} n_s = 1 &- \frac{4\,\mu\,\phi\,\beta\,\varphi^2 + 16\,\phi^n n\beta\,\varphi - 8\,\phi^n\varphi + 8\,\phi^{n+1}\mu - 2\,\phi^{-n}\varphi^5 + 2\,\phi^{-n}n\beta\,\varphi^5 - 10\,\phi^{-n}n\varphi^5}{4\phi(2\,\beta\,\phi^n+\varphi^2-2\,\phi^n)(\varphi^2-2\,\phi^n)} \\ &- \frac{-8\,\phi^{n+1}\mu\,\beta + \phi^{-2\,n}n\varphi^7 + 6\,\phi^{-n+1}\varphi^4\mu + 24\,\varphi^3 n - 12\,n\beta\,\varphi^3 - 16\,\phi^n n\varphi + 8\,\phi^n\beta\,\varphi - 16\,\varphi^2\mu\,\phi}{4\phi(2\,\beta\,\phi^n+\varphi^2-2\,\phi^n)(\varphi^2-2\,\phi^n)} \\ &- \frac{-4\,\beta\,\varphi^3+8\,\varphi^3}{4\phi(2\,\beta\,\phi^n+\varphi^2-2\,\phi^n)(\varphi^2-2\,\phi^n)}, \end{aligned} \tag{75}$$

$$n_T = -\frac{n^2(16\,\phi^{n-2}n^2\beta^3 - 24\,\phi^{n-2}n^2\beta^2 + 12\,\phi^{n-2}n^2\beta - 2\,\phi^{n-2}n^2 - 2\,\beta + 1)}{\phi^2}, \tag{76}$$

and

$$r = 8\,\frac{n^2(2\,\kappa^4\beta-1)(8\,\phi^{n-2}n^2\kappa^8\beta^2 - 8\,\phi^{n-2}n^2\beta\kappa^4 + \kappa^4\beta - \kappa^4 + 2\,\phi^{n-2}n^2)}{\kappa^6\phi^2}, \tag{77}$$

with

$$\varphi = 2\,\phi^{n-1}n(2\,\beta-1) \tag{78}$$

and

$$\mu = 2\,\phi^{n-2}n(2\,\beta\,n - n - 2\,\beta + 1). \tag{79}$$

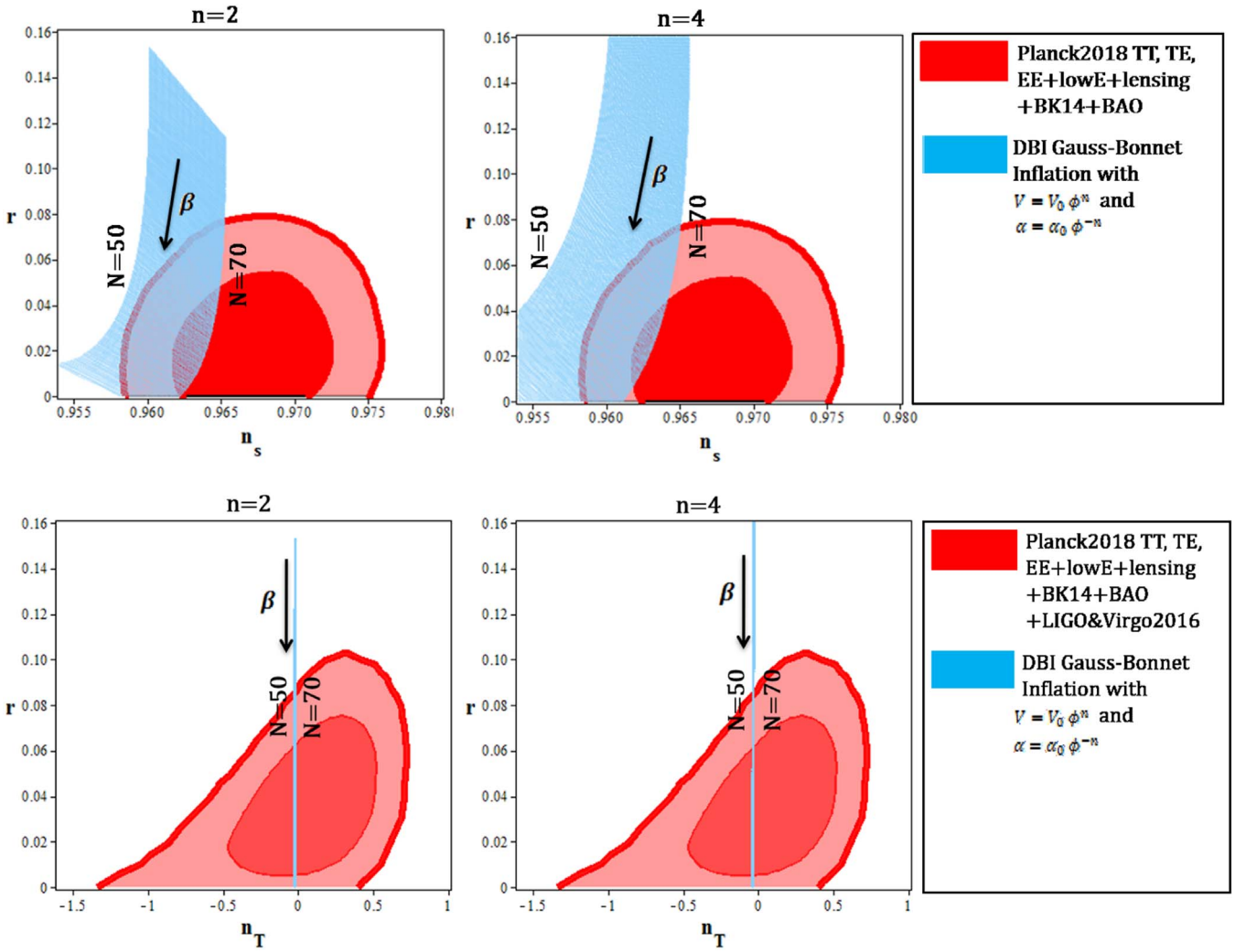

Figure 7. Tensor-to-scalar ratio vs. the scalar spectral index and tensor spectral index of the DBI GB model with $V = V_0\,\phi^n$ and $\mathcal{G} = \mathcal{G}_0\,\phi^{-n}$.

Table 6
The Ranges of the Parameter β in Which the Tensor-To-Scalar Ratio, the Scalar Spectral Index, and the Tensor Spectral Index of the Tachyon GB Model with $V = V_0\,\phi^n$ and $\mathcal{G} = \mathcal{G}_0\,e^{-\lambda\phi}$ Are Consistent with Different Data Sets

		Planck2018 TT, TE, EE+lowE +lensing+BK14+BAO	Planck2018 TT,TE,EE+lowE +lensing+BK14+BAO	Planck2018 TT, TE, EE+lowE lensing+BK14+BAO +LIGO and Virgo2016	Planck2018 TT, TE, EE+lowE lensing+BK14+BAO LIGO and Virgo2016
	N	68% CL	95% CL	68% CL	95% CL
$n = 2$	10	$\beta \leqslant 0.832$	All values of β	Not consistent	All values of β
	10^2	$0.421 \leqslant \beta \leqslant 0.683$	All values of β	$\beta \leqslant 0.742$	All values of β
	10^4	Not consistent	All values of β	$\beta \leqslant 0.839$	All values of β
$n = 4$	10	All values of β	All values of β	Not consistent	All values of β
	10^2	$0.093 \leqslant \beta$	All values of β	$\beta \leqslant 0.886$	All values of β
	10^4	$0.411 \leqslant \beta$	$0.046 \leqslant \beta$	$0.235 \leqslant \beta \leqslant 0.901$	All values of β

Performing an analysis on the above scalar spectral index and tensor-to-scalar ratio gives Figure 7. Our numerical analysis shows that the GB effect makes the DBI model observationally viable, but this viability happens with $N > 52$ for $n = 2$ and $N > 59$ for $n = 4$. The bottom panels of Figure 7 show the tensor spectral index versus the tensor-to-scalar ratio of the DBI GB model with $V = V_0\,\phi^n$ and $\mathcal{G} = \mathcal{G}_0\,\phi^{-n}$, in the background of the base+GW data. The ranges of the parameter β in which the scalar spectral index, the tensor spectral index, and the tensor-to-scalar ratio of this model are consistent with the base data at 68% CL and 95% CL are summarized in Table 7. These considerations show that the DBI GB inflation with $V = V_0\,\phi^n$

and $\mathcal{G} = \mathcal{G}_0\,\phi^{-n}$ for both $n = 2$ and $n = 4$ cases is consistent with observational data if $\beta \lesssim \mathcal{O}(10^{-1})$ and $N \gtrsim 60$.

7.2. Power-law Potential and Dilaton-like GB Coupling

In this section, we consider the following potential and GB coupling:

$$V = V_0\,\phi^n, \quad \mathcal{F} = \mathcal{F}_0\phi^{-n} \quad \text{and} \quad \mathcal{G} = \mathcal{G}_0\,e^{-\lambda\phi}, \tag{80}$$

which lead to

$$n_s = 1 - \frac{-\frac{nB}{\phi} + \frac{nA}{\phi\,\kappa^2}}{A^{-1}\kappa^2B^2} - 2\,\frac{n(-B\kappa^2 + A)(-2\,B^2C\phi^n\kappa^2 + 6\,AB^2C - A\phi^{n-1}n + A\phi^{n-1})}{B(-2\,nB\kappa^2 + 2\,nA + \beta\,\lambda\,e^{-\lambda\,\phi}\phi\,\kappa^2B^2)(-\phi^n\kappa^2 + A)} - \frac{\beta\,\lambda\,e^{-\lambda\,\phi}(2\,C\kappa^2B^2\phi - \lambda\,\phi\,A + 2\,nA)B}{-2\,nB\kappa^2 + 2\,nA + \beta\,\lambda\,e^{-\lambda\,\phi}\phi\,\kappa^2B^2}, \tag{81}$$

with

$$B = \phi^n + \frac{1}{\phi^{-n}}, \tag{82}$$

$$A = -\frac{nB}{\phi} + \kappa^4B^2\beta\,\lambda\,e^{-\lambda\,\phi}, \tag{83}$$

and

$$C = \frac{1}{2}\left(-\frac{Bn^2}{\phi^2} + \frac{nB}{\phi^2} + 2\,\frac{\kappa^4B^2\beta\,\lambda\,e^{-\lambda\,\phi}n}{\phi} - \kappa^4B^2\beta\,\lambda^2e^{-\lambda\,\phi}\right)\kappa^{-2}B^{-2} - \frac{An}{B^2\phi\,\kappa^2}. \tag{84}$$

The tensor spectral index is given by

$$n_T = -\frac{n(n\phi\,\kappa^2 - 2\,\phi^{n+2}\kappa^6\beta\lambda\,e^{-\lambda\,\phi} + n^2 - 4\,\phi^{n+1}n\kappa^4\beta\,\lambda\,e^{-\lambda\,\phi} + 4\,\phi^{2\,n+2}\kappa^8\beta^2\lambda^2e^{-2\,\lambda\,\phi})}{\kappa^4\phi^3}. \tag{85}$$

The tensor-to-scalar ratio takes the following form:

$$r = 8\,\frac{n^2\phi\,\kappa^2 - 2\,\phi^{n+2}n\kappa^6\beta\,\lambda\,e^{-\lambda\,\phi} + n^3 - 4\,\phi^{n+1}n^2\kappa^4\beta\,\lambda\,e^{-\lambda\,\phi} + 4\,\phi^{2n+2}n\kappa^8\beta^2\lambda^2e^{-2\,\lambda\,\phi}}{\kappa^4\phi^3} + 8\,\frac{2\,\beta^2\lambda^2e^{-2\,\lambda\,\phi}\kappa^6\phi^{3+2\,n} - \beta\,\lambda\,e^{-\lambda\,\phi}\kappa^2\phi^{n+2}n}{\kappa^4\phi^3}. \tag{86}$$

Now, we analyze these perturbation parameters numerically, and the results are shown in Figure 8. Our numerical analysis shows that the GB effect makes the DBI model observationally viable. The ranges of the parameter β in which both the scalar spectral index and the tensor-to-scalar ratio of this model are consistent with the base and base+GW data at 68% CL and 95% CL are summarized in Table 8. These considerations show that the DBI GB inflation with $V = V_0\,\phi^n$ and $\mathcal{G} = \mathcal{G}_0\,e^{-\lambda\phi}$ for both $n = 2$ and $n = 4$ cases is consistent with observational data if $\beta \lesssim \mathcal{O}(10^{-1})$.

8. Reheating Phase in a GB Model with a Canonical Scalar Field

The reheating process after inflation is necessary to reheat the universe for subsequent evolution. Actually, this process can explain the cosmic origin of the matter component of the universe (Kofman et al. 1994; Kofman 1996). The production of cosmic relics, such as photons and neutrinos, can be explained by considering the process of reheating in the universe (Giudice et al. 1999; Wallisch 2018). Also, the reheating phase accounts for the observed matter–antimatter asymmetry in the universe (Dine & Kusenko 2004; Lozanov & Amin 2014). By studying the reheating process in the GB models, we can find more constraints on the model's parameter space. To study this process, we focus on two important parameters $N_{\rm rh}$ and $T_{\rm rh}$ (where subscript rh stands for reheating). We obtain some expressions for these parameters in terms of the scalar spectral index, which let us compare the model with observational data (see Dai et al. 2014; Cook et al. 2015; Munoz & Kamionkowski 2015; Ueno & Yamamoto 2016). By using the expression

$$N_{\rm hc} = \ln\left(\frac{a_e}{a_{\rm hc}}\right), \tag{87}$$

we define the e-folds number between the time when the physical scales cross the horizon and the time when the inflation ends. The subscripts hc and e show the value of the parameter at the horizon crossing and end of inflation, respectively. For the energy density during the reheating epoch, we have the relation $\rho \sim a^{-3(1+\omega_{\rm eff})}$, with $\omega_{\rm eff}$ being the effective equation of state corresponding to the dominant energy density in the universe. Therefore, the e-folds number is

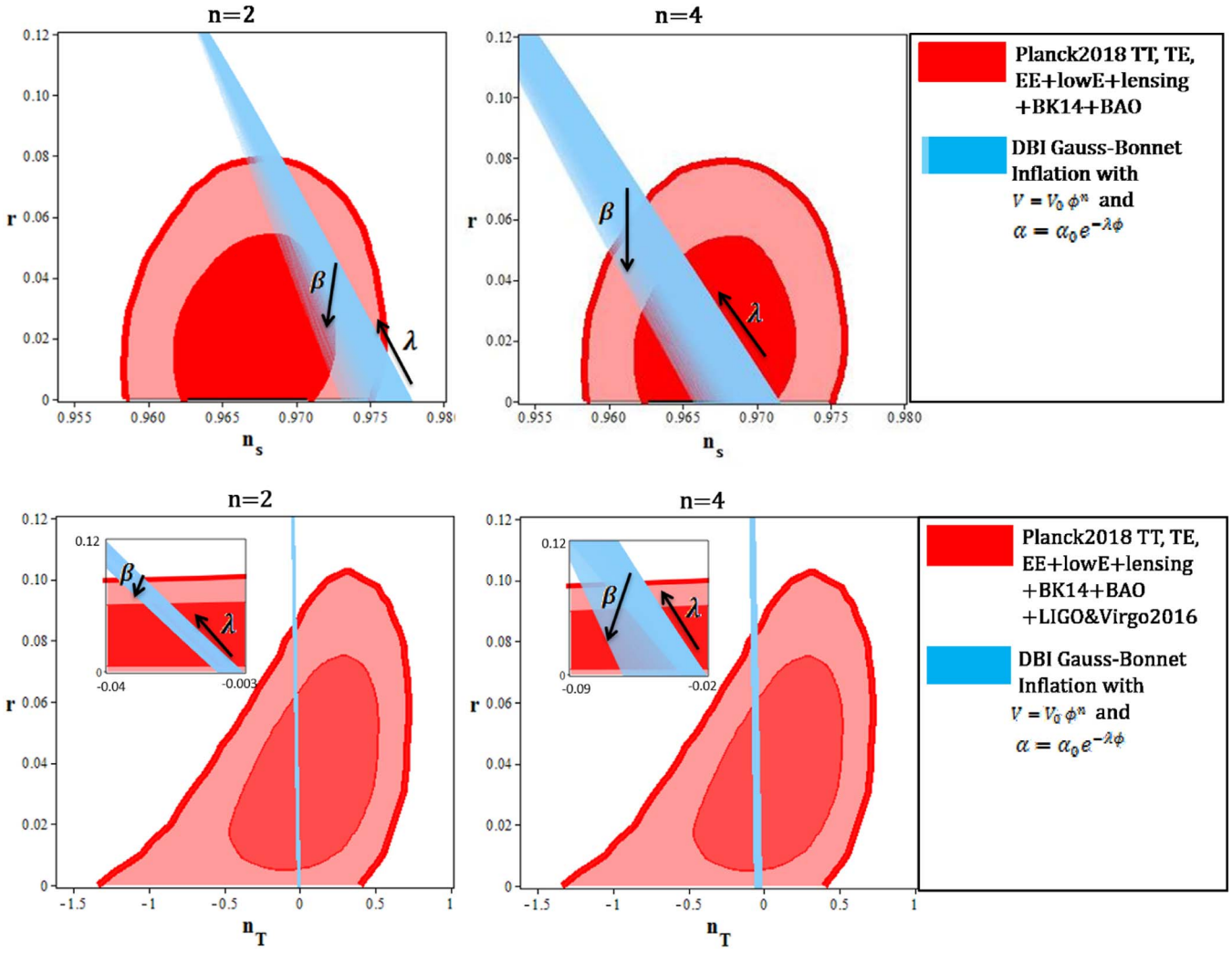

Figure 8. Tensor-to-scalar ratio vs. the scalar spectral index and tensor spectral index of the DBI GB model with $V = V_0\,\phi^n$ and $\mathcal{G} = \mathcal{G}_0\,e^{-\lambda\phi}$.

written in terms of ρ and $\omega_{\rm eff}$ as follows:

$$N_{\rm rh} = \ln\left(\frac{a_{\rm rh}}{a_e}\right) = -\frac{1}{3(1+\omega_{\rm eff})}\ln\left(\frac{\rho_{\rm rh}}{\rho_e}\right). \tag{88}$$

At the horizon crossing ($k = aH$) we have

$$0 = \ln\left(\frac{k_{\rm hc}}{a_{\rm hc}\,H_{\rm hc}}\right) = \ln\left(\frac{a_e}{a_{\rm hc}}\frac{a_{\rm rh}}{a_e}\frac{a_0}{a_{\rm rh}}\frac{k_{\rm hc}}{a_0 H_{\rm hc}}\right), \tag{89}$$

where the subscript 0 shows the value of the scale factor at the current time. From Equations (42)–(44) we obtain

$$N_{\rm hc} + N_{\rm rh} + \ln\left(\frac{k_{\rm hc}}{a_0 H_{\rm hc}}\right) + \ln\left(\frac{a_0}{a_{\rm rh}}\right) = 0. \tag{90}$$

To rewrite $\frac{a_0}{a_{\rm rh}}$ in terms of temperature and density, we use the following expression (Cook et al. 2015; Ueno & Yamamoto 2016):

$$\rho_{\rm rh} = \frac{\pi^2 g_{\rm rh}}{30} T_{\rm rh}^4, \tag{91}$$

where the parameter $g_{\rm rh}$ is the effective number of the relativistic species at the reheating era. Also, the conservation of the entropy gives (Cook et al. 2015; Ueno & Yamamoto 2016)

$$\frac{a_0}{a_{\rm rh}} = \left(\frac{43}{11 g_{\rm rh}}\right)^{-\frac{1}{3}}\frac{T_{\rm rh}}{T_0}, \tag{92}$$

where the subscript 0 denotes the current value of the temperature. Now, from Equations (91) and (92), we find the following expression for the scale factor:

$$\frac{a_0}{a_{\rm rh}} = \left(\frac{43}{11 g_{\rm rh}}\right)^{-\frac{1}{3}} T_0^{-1}\left(\frac{\pi^2 g_{\rm rh}}{30\rho_{\rm rh}}\right)^{-\frac{1}{4}}. \tag{93}$$

In the GB model with a canonical scalar field, we can write the energy density as follows:

$$\rho = \left(1+\frac{\epsilon}{3}\right)V - \frac{160}{27}\kappa^6\alpha'^2\,V^3 - \frac{20}{9}\kappa^2\alpha' V' V. \tag{94}$$

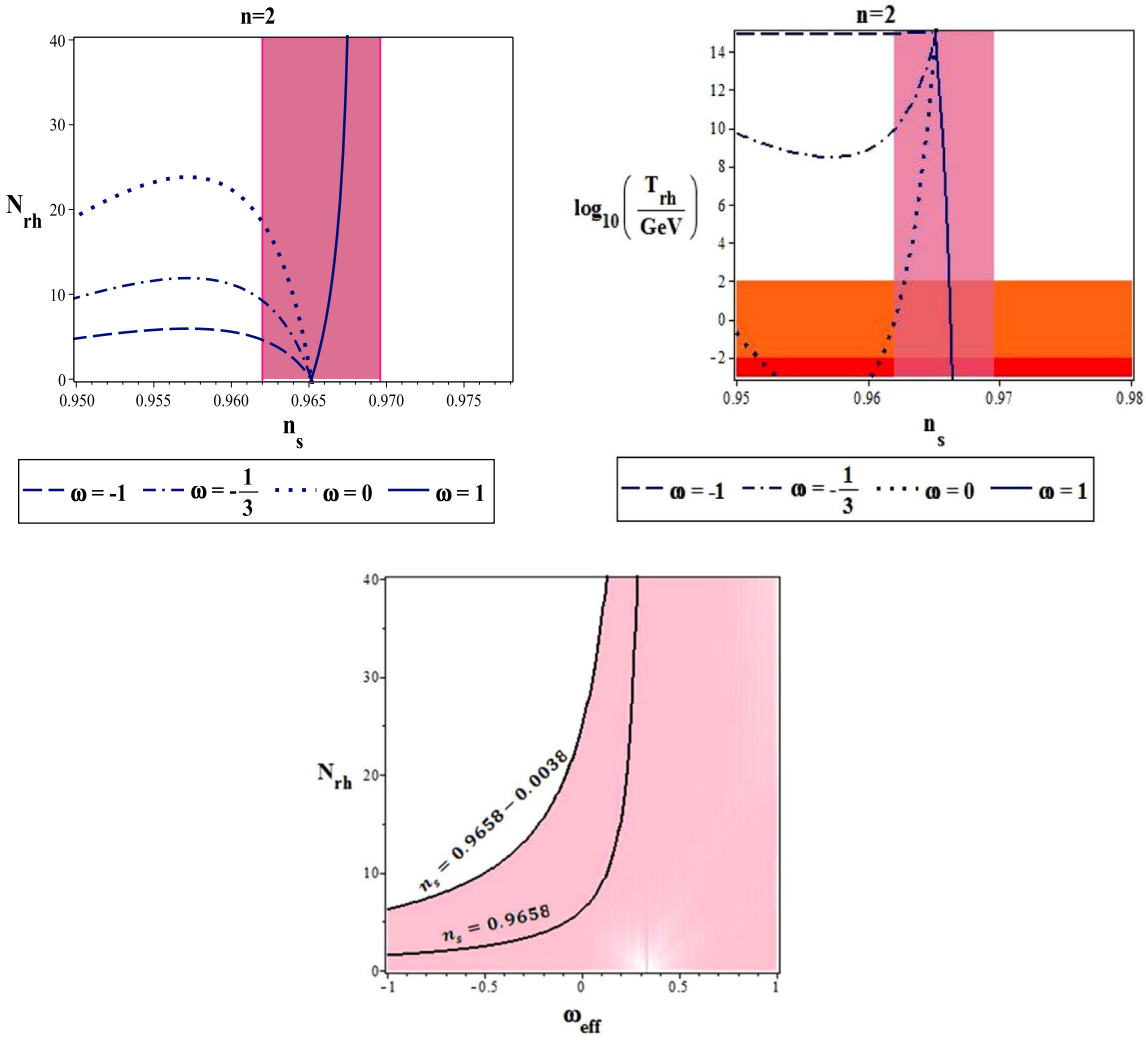

Figure 9. Behavior of the e-folds number (top left panel) and temperature (top right panel) during the reheating phase vs. the scalar spectral index, and the range of $N_{\rm rh}$ and $\omega_{\rm eff}$ leading to the observationally viable values of the scalar spectral index (bottom panel), in the GB model with a canonical scalar field and with $V = V_0\,\phi^2$ and $\mathcal{G} = \mathcal{G}_0\,\phi^{-2}$. The magenta region in the top panels shows the values of the scalar spectral index released by Planck2018 TT, TE, EE+lowE+lensing+BK14+BAO joint data. In the top right panel, the orange region corresponds to the temperatures below the electroweak scale, $T < 100$ GeV, and the red region corresponds to the temperatures below the big bang nucleosynthesis scale, $T < 10$ MeV.

Table 7
The Ranges of the Parameter β in which the Tensor-to-Scalar Ratio, the Scalar Spectral Index, and the Tensor Spectral Index of the DBI GB Model with $V = V_0\,\phi^n$ and $\mathcal{G} = \mathcal{G}_0\,\phi^{-n}$ Are Consistent with Different Data Sets

		Planck2018 TT, TE, EE+lowE +lensing+BK14+BAO	Planck2018 TT, TE, EE+lowE +lensing+BK14+BAO	Planck2018 TT, TE, EE+lowE lensing+BK14+BAO +LIGO and Virgo2016	Planck2018 TT, TE, EE+lowE lensing+BK14+BAO LIGO and Virgo2016
	N	68% CL	95% CL	68% CL	95% CL
$n = 2$	50	Not consistent	Not consistent	$0.617 \leqslant \beta < 1$	$0.411 \leqslant \beta < 1$
	60	Not consistent	$0.613 \leqslant \beta \leqslant 0.948$	$0.607 \leqslant \beta < 1$	$0.352 \leqslant \beta < 1$
	70	$0.705 \leqslant \beta \leqslant 0.981$	$0.326 \leqslant \beta < 1$	$0.489 \leqslant \beta \leqslant 0.971$	$0.361 \leqslant \beta < 1$
$n = 4$	50	Not consistent	Not consistent	$0.733 \leqslant \beta < 1$	$0.674 \leqslant \beta < 1$
	60	Not consistent	$0.683 \leqslant \beta \leqslant 0.915$	$0.712 \leqslant \beta \leqslant 0.980$	$0.676 \leqslant \beta < 1$
	70	$0.774 \leqslant \beta \leqslant 0.865$	$0.643 \leqslant \beta < 1$	$0.702 \leqslant \beta \leqslant 0.984$	$0.680 \leqslant \beta < 1$

To obtain the energy density at the end of the inflation era, we set $\epsilon = 1$. Then, we find

$$\rho_e = \frac{4}{3}V_e - \frac{160}{27}\kappa^6\alpha_e'^2\,V_e^3 - \frac{20}{9}\kappa^2\alpha_e' V_e'\,V_e. \tag{95}$$

Now, by using Equations (88) and (95), we obtain

$$\rho_{\rm rh} = \left[\frac{4}{3}V_e - \frac{160}{27}\kappa^6\alpha_e'^2\,V_e^3 - \frac{20}{9}\kappa^2\alpha_e' V_e'\,V_e\right] \times \exp\left[-3N_{\rm rh}(1+\omega_{\rm eff})\right]. \tag{96}$$

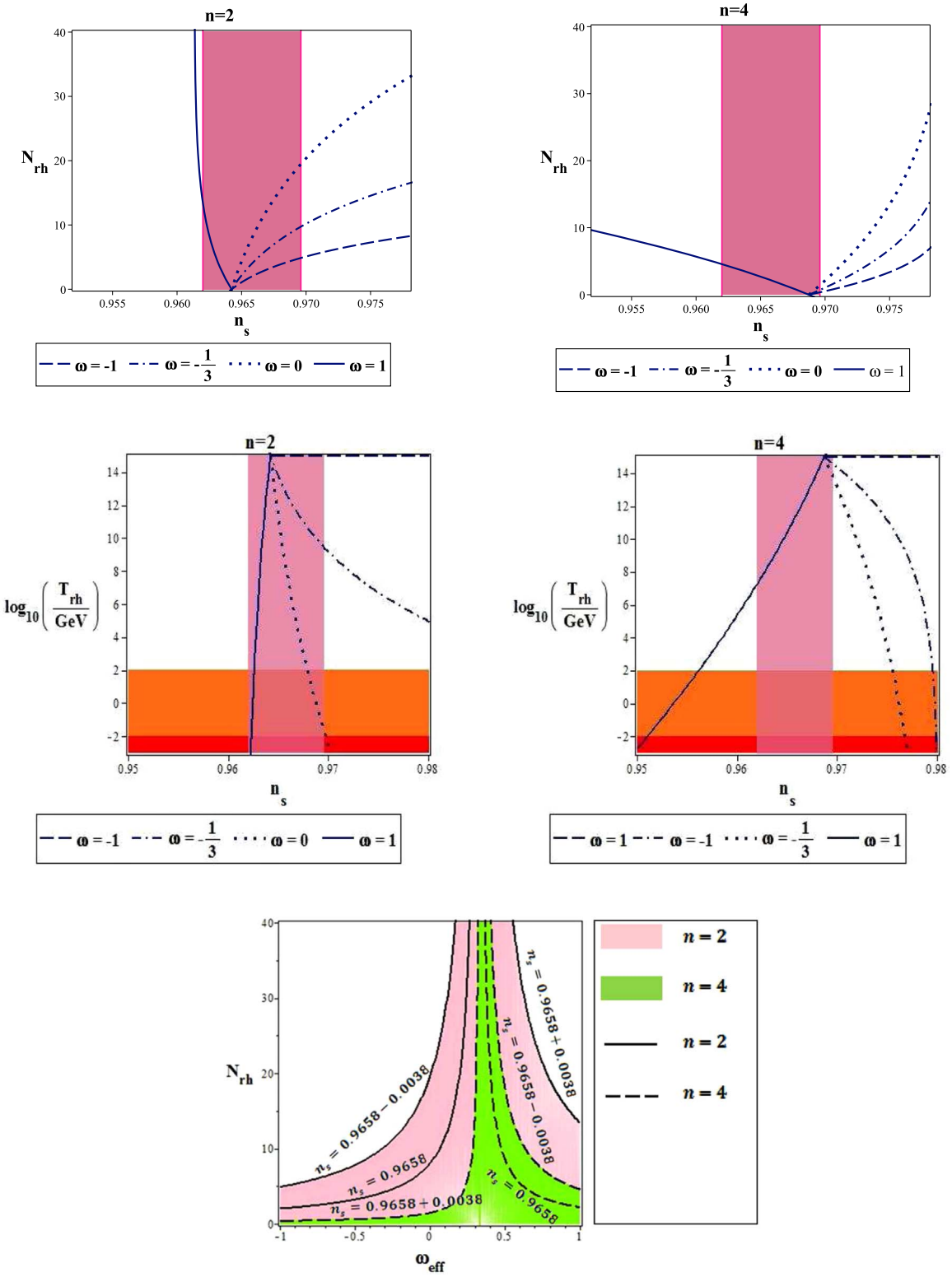

Figure 10. Behavior of the e-folds number (top panels) and temperature (middle panels) during the reheating phase vs. the scalar spectral index, and the range of $N_{\rm rh}$ and $\omega_{\rm eff}$ leading to the observationally viable values of the scalar spectral index (bottom panel), in the GB model with a canonical scalar field and with $V = V_0\,\phi^2$ and $\mathcal{G} = \mathcal{G}_0\,e^{-\lambda\phi}$.

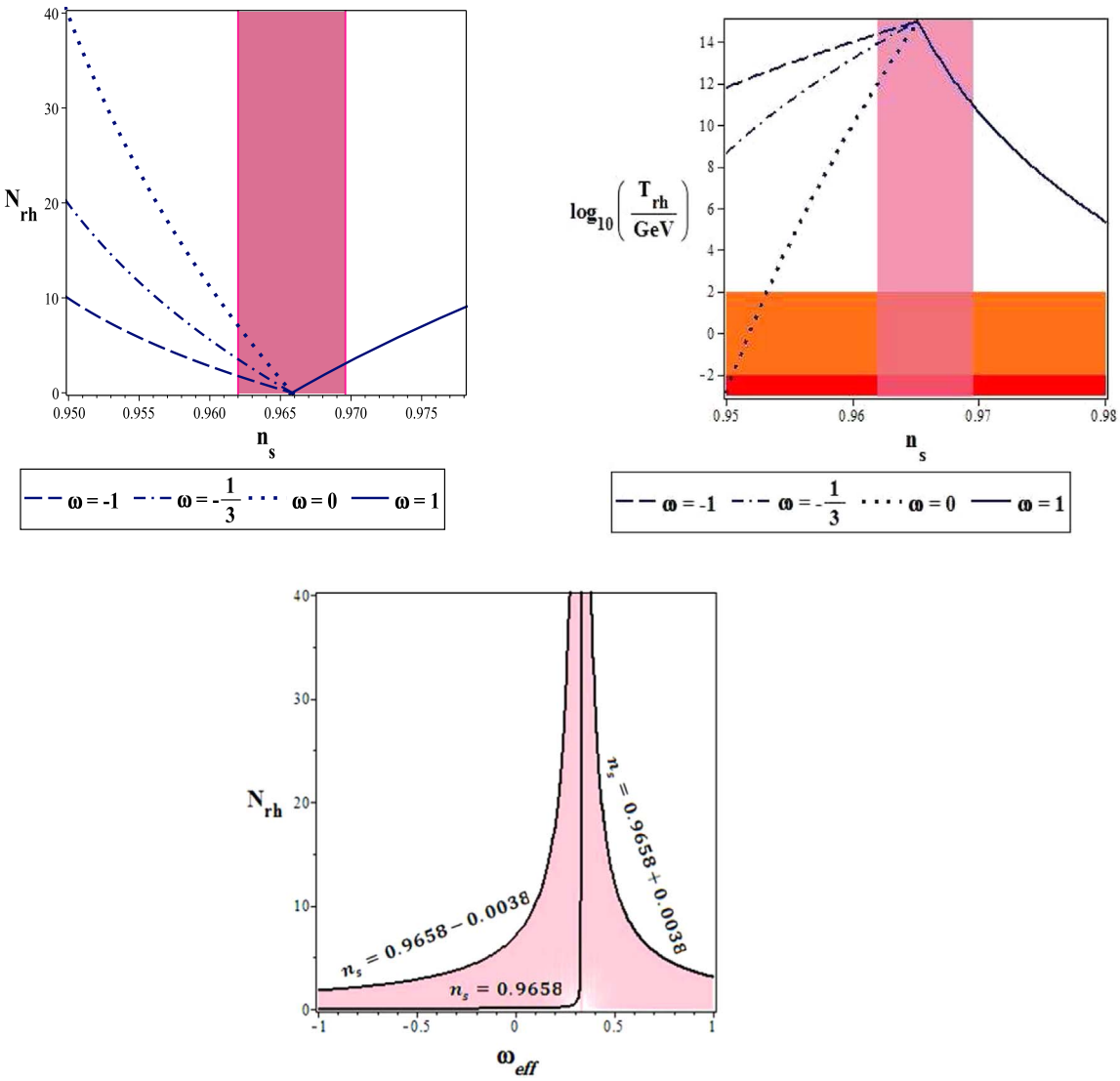

Figure 11. Behavior of the e-folds number (top left panel) and temperature (top right panel) during the reheating phase vs. the scalar spectral index, and the range of $N_{\rm rh}$ and $\omega_{\rm eff}$ leading to the observationally viable values of the scalar spectral index (bottom panel), in the GB natural inflation.

Table 8
The Ranges of the Parameter β in Which the Tensor-to-Scalar Ratio, the Scalar Spectral Index, and the DBI GB Model with $V = V_0\,\phi^n$ and $\mathcal{G} = \mathcal{G}_0\,e^{-\lambda\phi}$ Are Consistent with Different Data Sets

		Planck2018 TT, TE, EE+lowE +lensing+BK14+BAO	Planck2018 TT, TE, EE+lowE +lensing+BK14+BAO	Planck2018 TT, TE, EE+lowE lensing+BK14+BAO +LIGO and Virgo2016	Planck2018 TT, TE, EE+lowE lensing+BK14+BAO LIGO and Virgo2016
	N	68% CL	95% CL	68% CL	95% CL
$n = 2$	10	Not consistent	$0.112 \leqslant \beta \leqslant 0.986$	$0.609 \leqslant \beta \leqslant 0.973$	$0.332 \leqslant \beta < 1$
	10^2	$0.917 \leqslant \beta < 1$	All values	$0.607 \leqslant \beta \leqslant 0.970$	$0.329 \leqslant \beta < 1$
	10^4	Not consistent	$0.326 \leqslant \beta < 1$	$0.601 \leqslant \beta \leqslant 0.966$	$0.321 \leqslant \beta < 1$
$n = 4$	10	All values	All values	$0.521 \leqslant \beta \leqslant 0.971$	$0.388 \leqslant \beta < 1$
	10^2	$0.182 \leqslant \beta < 1$	All values	$0.518 \leqslant \beta \leqslant 0.969$	$0.381 \leqslant \beta < 1$
	10^4	Not consistent	$0.442 \leqslant \beta < 1$	$0.511 \leqslant \beta \leqslant 0.965$	$0.370 \leqslant \beta < 1$

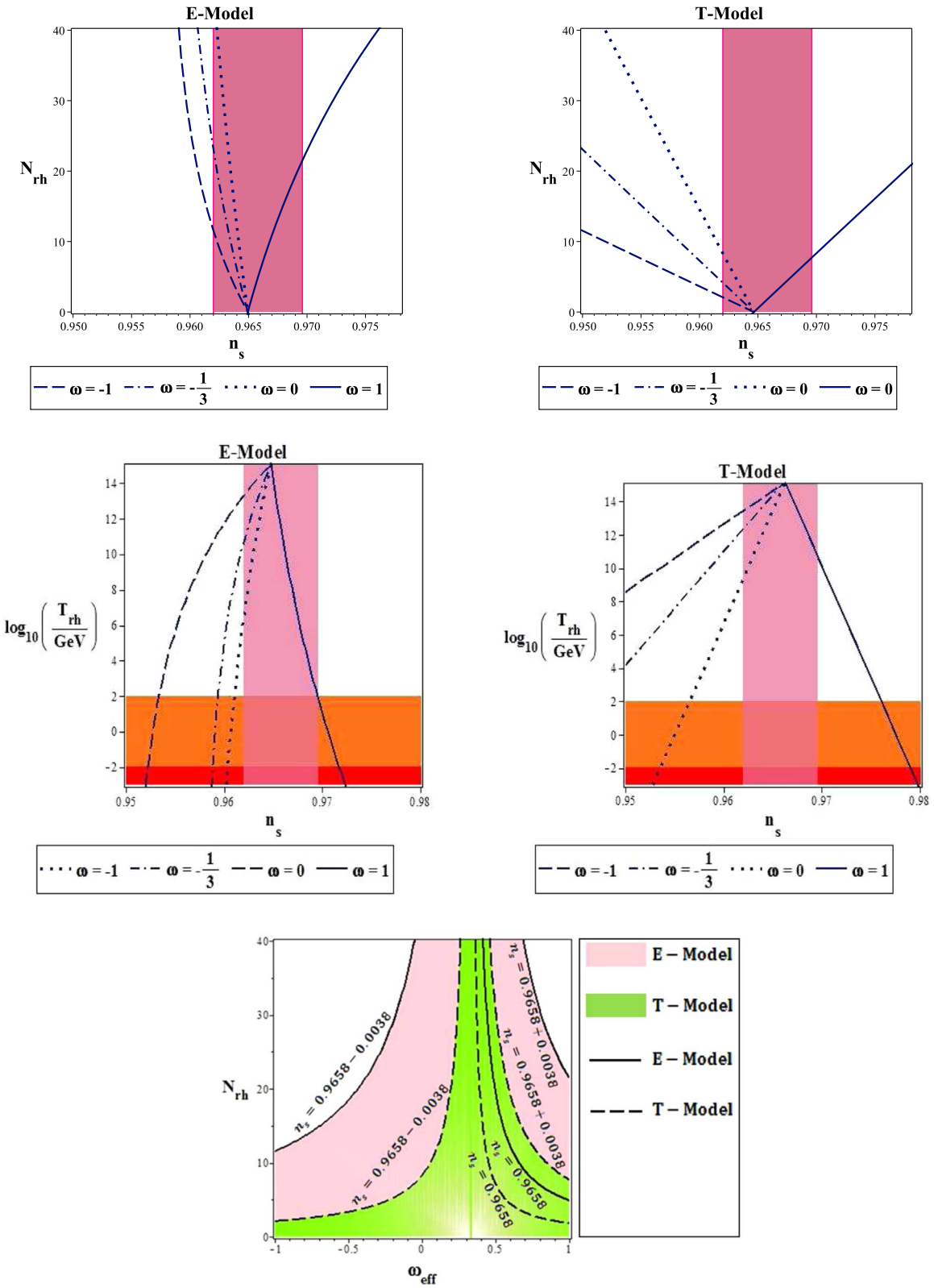

Figure 12. Behavior of the *e*-folds number (top panels) and temperature (middle panels) during the reheating phase vs. the scalar spectral index, and the range of $N_{\rm rh}$ and $\omega_{\rm eff}$ leading to the observationally viable values of the scalar spectral index (bottom panel), in the GB α-attractor model.

Table 9
Constraints on the e-folds Number and Temperature during the Reheating Phase in the GB Model with a Canonical Scalar Field and with $V = V_0\,\phi^n$ and $\mathcal{G} = \mathcal{G}_0\,\phi^{-n}$, Obtained from Planck2018 TT, TE, EE+lowE+lensing+BK14+BAO Joint Data

		$\omega = -1$	$\omega = -\frac{1}{3}$	$\omega = 0$	$\omega = 1$
$n = 2$	$0.680 \leqslant \beta < 1$	$N_{\rm rh} < 7.4$	$N_{\rm rh} < 12.37$	$N_{\rm rh} < 23.35$	All values of $N_{\rm rh}$
$n = 2$	$0.680 \leqslant \beta < 1$	$\log_{10}\left(\frac{T_{\rm rh}}{\rm GeV}\right) > 14.16$	$\log_{10}\left(\frac{T_{\rm rh}}{\rm GeV}\right) > 7.96$	$\log_{10}\left(\frac{T_{\rm rh}}{\rm GeV}\right) > -0.73$	All values of $T_{\rm rh}$

Table 10
Constraints on the e-folds Number and Temperature during the Reheating Phase in the GB Model with a Canonical Scalar Field and with $V = V_0\,\phi^n$ and $\mathcal{G} = \mathcal{G}_0\,e^{-\lambda\phi}$, Obtained from Planck2018 TT, TE, EE+lowE+lensing+BK14+BAO Joint Data

		$\omega = -1$	$\omega = -\frac{1}{3}$	$\omega = 0$	$\omega = 1$
$n = 2$	$0.031 \leqslant \beta < 0.072$	$N_{\rm rh} < 6.85$	$N_{\rm rh} < 11.47$	$N_{\rm rh} < 22.66$	$N_{\rm rh} < 16.72$
$n = 4$	$0.670 \leqslant \beta \leqslant 0.716$	$N_{\rm rh} < 0.56$	$N_{\rm rh} < 1.42$	$N_{\rm rh} < 2.37$	$N_{\rm rh} < 5.14$
$n = 2$	$0.031 \leqslant \beta < 0.072$	$\log_{10}\left(\frac{T_{\rm rh}}{\rm GeV}\right) > 14.09$	$\log_{10}\left(\frac{T_{\rm rh}}{\rm GeV}\right) > 8.65$	$\log_{10}\left(\frac{T_{\rm rh}}{\rm GeV}\right) > -2.21$	All values of $T_{\rm rh}$
$n = 4$	$0.670 \leqslant \beta \leqslant 0.716$	$\log_{10}\left(\frac{T_{\rm rh}}{\rm GeV}\right) > 14.18$	$\log_{10}\left(\frac{T_{\rm rh}}{\rm GeV}\right) > 14.53$	$\log_{10}\left(\frac{T_{\rm rh}}{\rm GeV}\right) > 13.22$	$\log_{10}\left(\frac{T_{\rm rh}}{\rm GeV}\right) > 6.27$

Table 11
Constraints on the e-folds Number and Temperature during the Reheating Phase in the GB Natural Inflation, Obtained from Planck2018 TT, TE, EE+lowE+lensing +BK14+BAO Joint Data

	$\omega = -1$	$\omega = -\frac{1}{3}$	$\omega = 0$	$\omega = 1$
$0.525 \leqslant \beta < 1$	$N_{\rm rh} < 2.85$	$N_{\rm rh} < 4.84$	$N_{\rm rh} < 10.42$	$N_{\rm rh} < 5.11$
$0.525 \leqslant \beta < 1$	$\log_{10}\left(\frac{T_{\rm rh}}{\rm GeV}\right) > 14.04$	$\log_{10}\left(\frac{T_{\rm rh}}{\rm GeV}\right) > 12.95$	$\log_{10}\left(\frac{T_{\rm rh}}{\rm GeV}\right) > 10.45$	$\log_{10}\left(\frac{T_{\rm rh}}{\rm GeV}\right) > 9.71$

Table 12
Constraints on the e-folds Number and Temperature during the Reheating Phase in the GB α-Attractor Model, Obtained from Planck2018 TT, TE, EE+lowE+lensing +BK14+BAO Joint Data

		$\omega = -1$	$\omega = -\frac{1}{3}$	$\omega = 0$	$\omega = 1$
E-model	$\beta \leqslant 4.81 \times 10^{-2}$	$N_{\rm rh} \leqslant 16.825$	$N_{\rm rh} \leqslant 37.521$	$N_{\rm rh} \leqslant 52.647$	$N_{\rm rh} \leqslant 26.367$
T-model	$\beta \leqslant 7.01 \times 10^{-2}$	$N_{\rm rh} \leqslant 4.110$	$N_{\rm rh} \leqslant 7.334$	$N_{\rm rh} \leqslant 12.45$	$N_{\rm rh} \leqslant 10.14$
E-model	$\beta \leqslant 4.81 \times 10^{-2}$	$\log_{10}\left(\frac{T_{\rm rh}}{\rm GeV}\right) \geqslant 12.49$	$\log_{10}\left(\frac{T_{\rm rh}}{\rm GeV}\right) \geqslant 8.73$	$\log_{10}\left(\frac{T_{\rm rh}}{\rm GeV}\right) \geqslant 4.73$	$\log_{10}\left(\frac{T_{\rm rh}}{\rm GeV}\right) \geqslant 0.266$
T-model	$\beta \leqslant 7.01 \times 10^{-2}$	$\log_{10}\left(\frac{T_{\rm rh}}{\rm GeV}\right) \geqslant 12.66$	$\log_{10}\left(\frac{T_{\rm rh}}{\rm GeV}\right) \geqslant 10.21$	$\log_{10}\left(\frac{T_{\rm rh}}{\rm GeV}\right) \geqslant 7.12$	$\log_{10}\left(\frac{T_{\rm rh}}{\rm GeV}\right) \geqslant 8.37$

Table 13
Constraints on the e-folds Number and Temperature during the Reheating Phase in the Tachyon GB Model with $V = V_0\,\phi^n$ and $\mathcal{G} = \mathcal{G}_0\,\phi^{-n}$, Obtained from Planck2018 TT, TE, EE+lowE+lensing+BK14+BAO Joint Data

		$\omega = -1$	$\omega = -\frac{1}{3}$	$\omega = 0$	$\omega = 1$
$n = 2$	$0.251 \leqslant \beta < 1$	$N_{\rm rh} \leqslant 5.65$	$N_{\rm rh} \leqslant 9.86$	$N_{\rm rh} \leqslant 19.62$	Not consistent
$n = 4$	$0.254 \leqslant \beta < 1$	$N_{\rm rh} \leqslant 4.73$	$N_{\rm rh} \leqslant 7.88$	$N_{\rm rh} \leqslant 15.87$	Not consistent
$n = 2$	$0.251 \leqslant \beta < 1$	$\log_{10}\left(\frac{T_{\rm rh}}{\rm GeV}\right) \geqslant 12.59$	$\log_{10}\left(\frac{T_{\rm rh}}{\rm GeV}\right) \geqslant 8.62$	$\log_{10}\left(\frac{T_{\rm rh}}{\rm GeV}\right) \geqslant 2.54$	Not consistent
$n = 4$	$0.254 \leqslant \beta < 1$	$\log_{10}\left(\frac{T_{\rm rh}}{\rm GeV}\right) \geqslant 12.03$	$\log_{10}\left(\frac{T_{\rm rh}}{\rm GeV}\right) \geqslant 9.42$	$\log_{10}\left(\frac{T_{\rm rh}}{\rm GeV}\right) \geqslant 15.87$	Not consistent

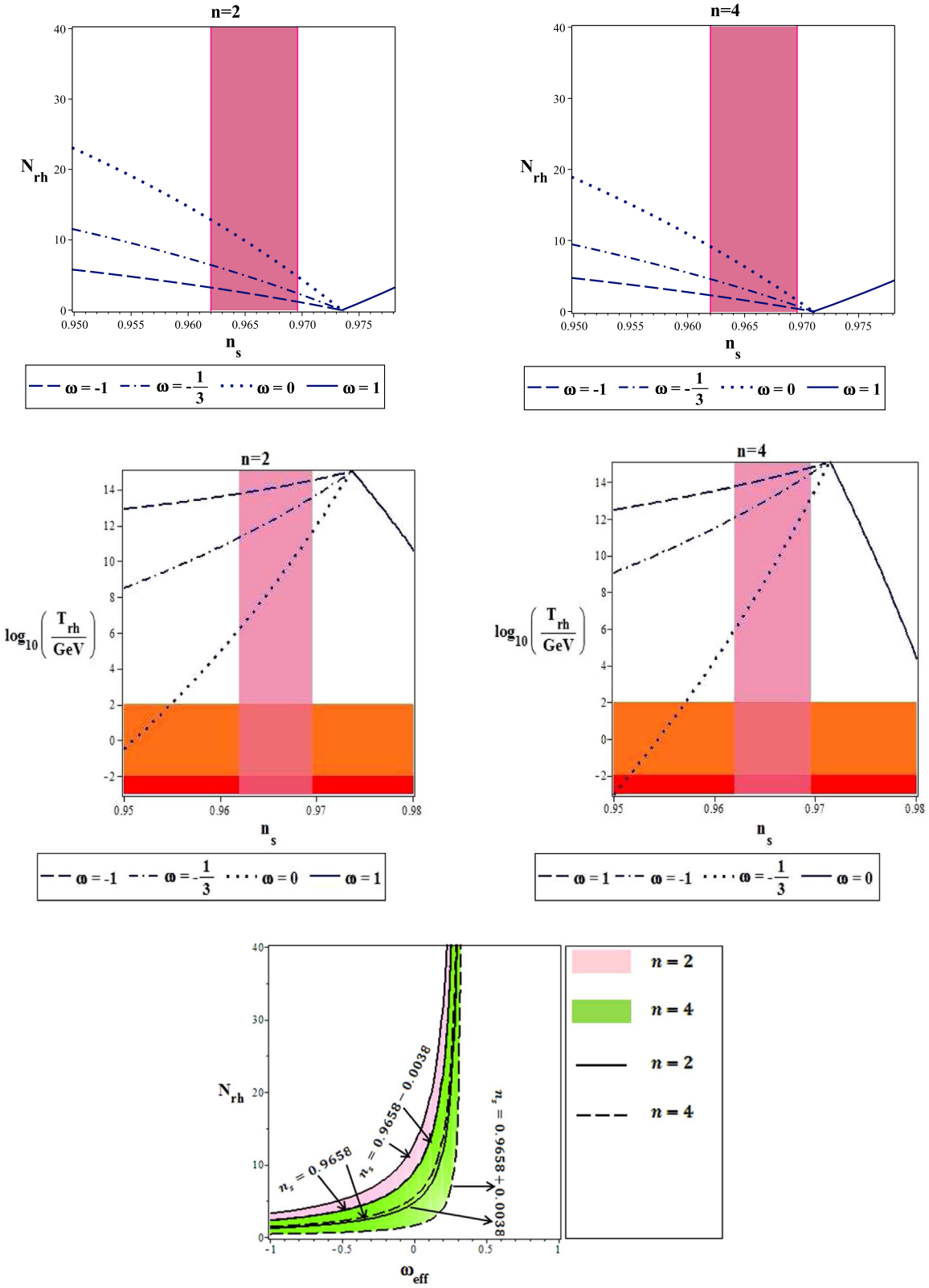

Figure 13. Behavior of the e-folds number (top panels) during the reheating phase vs. the scalar spectral index, and the range of $N_{\rm rh}$ and $\omega_{\rm eff}$ leading to the observationally viable values of the scalar spectral index (bottom panel), in the tachyon GB model with $V = V_0\,\phi^n$ and $\mathcal{G} = \mathcal{G}_0\,\phi^{-n}$.

Table 14
Constraints on the e-folds Number and Temperature during the Reheating Phase in the Tachyon GB Model with $V = V_0\,\phi^n$ and $\mathcal{G} = \mathcal{G}_0\,e^{-\lambda\phi}$, Obtained from Planck2018 TT, TE, EE+lowE+lensing+BK14+BAO Joint Data

	β	$\omega = -1$	$\omega = -\frac{1}{3}$	$\omega = 0$	$\omega = 1$
$n = 2$	$0.023 \leqslant \beta < 1$	$N_{\rm rh} \leqslant 5.73$	$N_{\rm rh} \leqslant 12.39$	$N_{\rm rh} \leqslant 20.04$	$N_{\rm rh} \leqslant 16.42$
$n = 4$	$0.046 \leqslant \beta < 1$	$N_{\rm rh} \leqslant 4.23$	$N_{\rm rh} \leqslant 8.11$	$N_{\rm rh} \leqslant 14.81$	$N_{\rm rh} \leqslant 17.76$
$n = 2$	$0.023 \leqslant \beta < 1$	$\log_{10}\left(\frac{T_{\rm rh}}{\rm GeV}\right) \geqslant 11.480$	$\log_{10}\left(\frac{T_{\rm rh}}{\rm GeV}\right) \geqslant 7.41$	$\log_{10}\left(\frac{T_{\rm rh}}{\rm GeV}\right) \geqslant 3.11$	$\log_{10}\left(\frac{T_{\rm rh}}{\rm GeV}\right) \geqslant 6.53$
$n = 4$	$0.046 \leqslant \beta < 1$	$\log_{10}\left(\frac{T_{\rm rh}}{\rm GeV}\right) \geqslant 13.07$	$\log_{10}\left(\frac{T_{\rm rh}}{\rm GeV}\right) \geqslant 11.90$	$\log_{10}\left(\frac{T_{\rm rh}}{\rm GeV}\right) \geqslant 8.91$	$\log_{10}\left(\frac{T_{\rm rh}}{\rm GeV}\right) \geqslant 8.03$

By using Equations (93) and (96), we find the following expression for the scale factor:

$$\ln\left(\frac{a_0}{a_{\rm rh}}\right) = -\frac{1}{3}\ln\left(\frac{43}{11 g_{\rm rh}}\right) - \frac{1}{4}\ln\left(\frac{\pi^2 g_{\rm rh}}{30\rho_{\rm rh}}\right) - \ln T_0 - \frac{3}{4}N_{\rm rh}(1+\omega_{\rm eff}) + \frac{1}{4}\ln\left(\frac{4}{3}V_e - \frac{160}{27}\kappa^6\alpha_e'^2\,V_e^3 - \frac{20}{9}\kappa^2\alpha_e' V_e'\,V_e\right). \tag{97}$$

To obtain $N_{\rm rh}$, we find $H_{\rm hc}$ from Equation (14). After that, by using Equations (90) and (97), we obtain the e-folds number during reheating as follows:

$$N_{\rm rh} = \frac{4}{1-3\omega_{\rm eff}}\left[-N_{\rm hc} - \ln\left(\frac{k_{\rm hc}}{a_0 T_0}\right) - \frac{1}{4}\ln\left(\frac{40}{\pi^2 g_{\rm rh}}\right) + \frac{1}{2}\ln\left(8\pi^2\mathcal{A}_s\mathcal{W}_s c_s^3\right) - \frac{1}{3}\ln\left(\frac{11 g_{\rm rh}}{43}\right) - \frac{1}{4}\ln\left(\frac{4}{3}V_e - \frac{160}{27}\kappa^6\alpha_e'^2\,V_e^3 - \frac{20}{9}\kappa^2\alpha_e' V_e'\,V_e\right)\right]. \tag{98}$$

The temperature during reheating is obtained from Equations (88), (92), and (95) as follows:

$$T_{\rm rh} = \left(\frac{30}{\pi^2 g_{\rm rh}}\right)^{\frac{1}{4}}\left[\frac{4}{3}V_e - \frac{160}{27}\kappa^6\alpha_e'^2\,V_e^3 - \frac{20}{9}\kappa^2\alpha_e' V_e'\,V_e\right]^{\frac{1}{4}} \times \exp\left[-\frac{3}{4}N_{\rm rh}(1+\omega_{\rm eff})\right]. \tag{99}$$

To perform a numerical analysis, it is useful to write Equations (98) and (99) in terms of the scalar spectral index. To this end, we should specify the potential and GB coupling. In the following, we adopt the potential and GB coupling used in the previous sections and explore each case separately.

8.1. Power-law Potential and Inverse Power-law GB Coupling

In this case, we use the potential and GB coupling defined in Equation (29). As we have seen before, in this case the GB model only with $n = 2$ is consistent with the base data. Therefore, we use Equation (29) with $n = 2$, find the final values of the potential and GB coupling in terms of the scalar field at the horizon crossing, and substitute them in Equations (98) and (99). After that, we obtain the scalar field at horizon crossing in terms of the scalar spectral index. By considering the value of the scalar spectral index, obtained from the base data, we find some constraints on the e-folds number and temperature during the reheating phase. In studying the r–n_s behavior with Equation (19), the tightest constraint on β has been obtained as $0.680 \leqslant \beta < 1$. To numerically analyze the reheating phase, we use this constraint and four values of ω: $\omega = -1$, $-\frac{1}{3}$, 0, and 1. The results are presented in Table 9. The behavior of $N_{\rm rh}$ and $T_{\rm rh}$ versus n_s, for $\beta = 0.7$, is shown in Figure 9. Note that, as the top left panel of Figure 9 shows, all curves converge to $N_{\rm rh} = 0$ (corresponding to instantaneous reheating process) and $n_s = 0.965$, which is observationally viable from base data.

The bottom panel of Figure 9 shows the range of $N_{\rm rh}$ and $\omega_{\rm eff}$, in the case considered in this subsection, leading to the observationally viable values of the scalar spectral index. As the figure shows, when $\omega_{\rm eff}$ changes from -1 (field's potential domination) to $\frac{1}{3}$ (radiation domination), the values of $N_{\rm rh}$ increase. This means that the reheating phase of the universe is not instantaneous and lasts some e-folds.

The parameter $N_{\rm rh}$, which describes the duration of the reheating phase, is related to the scalar spectral index of the perturbations. To have a viable reheating phase, $N_{\rm rh}$ should be consistent with the observational value of n_s. Any small variation of $N_{\rm rh}$ can lead to values of n_s that are not observationally viable. Therefore, the reheating phase should last until some specific values and not more than it. In this regard, we have tried to obtain some precise values of the parameters leading to the viable GB models.

8.2. Power-law Potential and Dilaton-like GB Coupling

In this subsection, we use the potential and GB coupling defined in Equation (34). We have shown that in this case the GB model with both $n = 2$ and $n = 4$ in some ranges of the parameters is consistent with the observational data. By using the adopted potential and GB coupling, we study the e-folds number and temperature in the reheating phase numerically and find some constraints on these parameters in confrontation with the base data. To obtain the constraints, we use the ranges of β from Table 2. In the $n = 2$ case, the tightest constraint on β is $0.031 \leqslant \beta \leqslant 0.072$, and in the $n = 4$ case we have $0.670 \leqslant \beta \leqslant 0.716$. With these ranges of β, we obtain the constraints shown in Table 10. The behavior of $N_{\rm rh}$ and $T_{\rm rh}$ versus n_s, for $\beta = 0.7$, is shown in the top and middle panels of Figure 10.

The bottom panel of Figure 10 shows the range of $N_{\rm rh}$ and $\omega_{\rm eff}$, in the case considered in this subsection, leading to the observationally viable values of the scalar spectral index. In

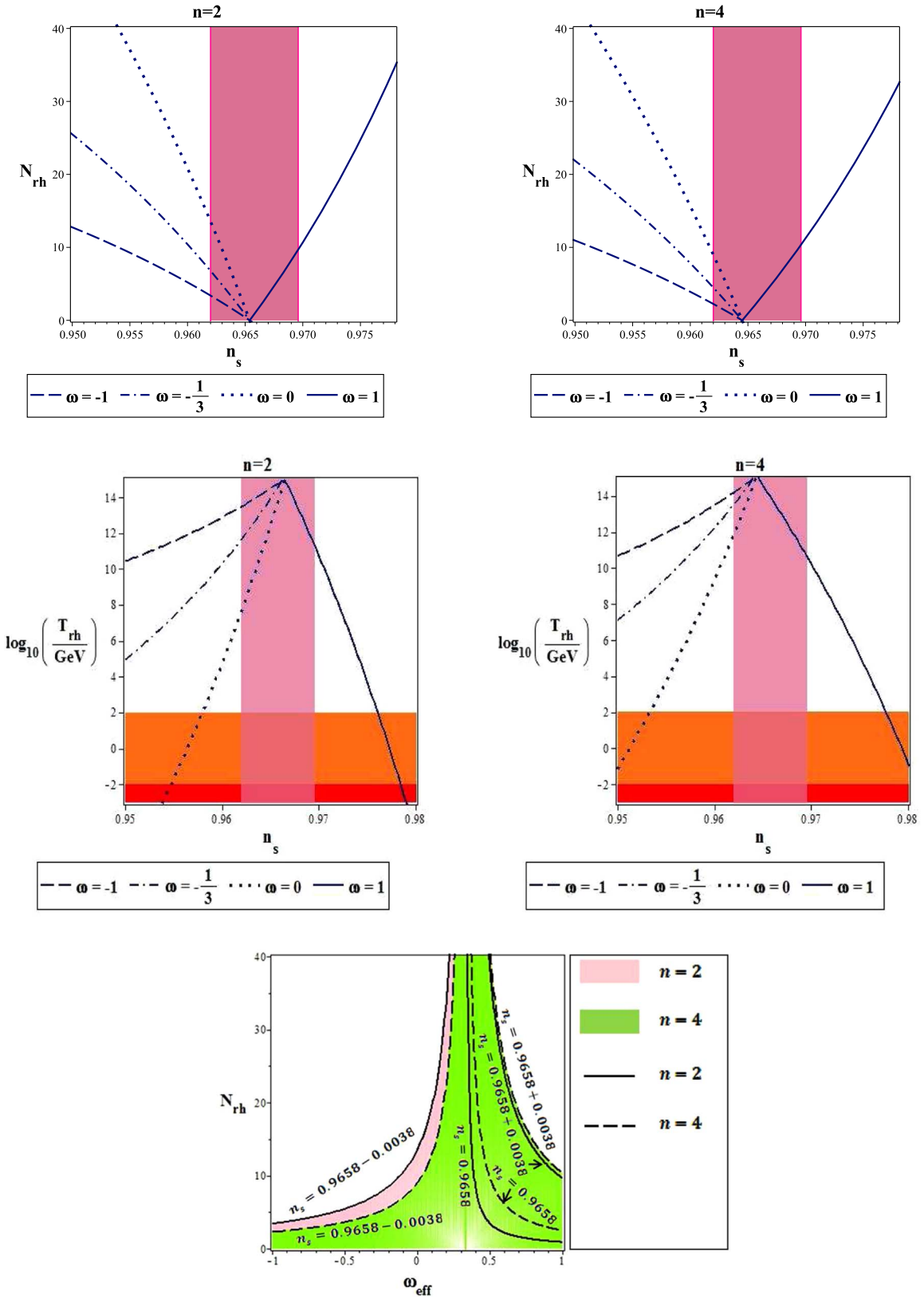

Figure 14. Behavior of the *e*-folds number (top panels) and temperature (middle panels) during the reheating phase vs. the scalar spectral index, and the range of $N_{\rm rh}$ and $\omega_{\rm eff}$ leading to the observationally viable values of the scalar spectral index (bottom panel), in the tachyon GB model with $V = V_0\,\phi^n$ and $\mathcal{G} = \mathcal{G}_0\,e^{-\lambda\phi}$.

this case also, when $\omega_{\rm eff}$ changes from -1 to $\frac{1}{3}$, the values of $N_{\rm rh}$ increase. This means that the reheating phase of the universe is not instantaneous and lasts some *e*-folds. However, this figure shows another point too. For $\omega_{\rm eff} > \frac{1}{3}$, by increasing the values of the effective equation-of-state parameter, the values of $N_{\rm rh}$ decrease. Therefore, in this case the value of $\omega_{\rm eff}$

Table 15
Constraints on the e-folds Number and Temperature during the Reheating Phase in the DBI GB Model with $V = V_0\,\phi^n$ and $\mathcal{G} = \mathcal{G}_0\,\phi^{-n}$, Obtained from Planck2018 TT, TE, EE+lowE+lensing+BK14+BAO Joint Data

		$\omega = -1$	$\omega = -\frac{1}{3}$	$\omega = 0$	$\omega = 1$
$n = 2$	$0.613 \leqslant \beta \leqslant 0.948$	$0.141 < N_{\rm rh} < 9.08$	$0.411 < N_{\rm rh} < 19.43$	$0.561 < N_{\rm rh} < 30.04$	Not consistent
$n = 4$	$0.683 \leqslant \beta \leqslant 0.915$	Not consistent	Not consistent	Not consistent	$1.86 < N < 52.14$
$n = 2$	$0.613 \leqslant \beta \leqslant 0.948$	$11.86 < \log_{10}\left(\frac{T_{\rm rh}}{\rm GeV}\right) < 14.97$	$9.12 < \log_{10}\left(\frac{T_{\rm rh}}{\rm GeV}\right) < 14.91$	$6.11 < \log_{10}\left(\frac{T_{\rm rh}}{\rm GeV}\right) < 14.86$	Not consistent
$n = 4$	$0.683 \leqslant \beta \leqslant 0.915$	Not consistent	Not consistent	Not consistent	$\log_{10}\left(\frac{T_{\rm rh}}{\rm GeV}\right) < 7.42$

does not become larger than $\frac{1}{3}$, because the e-folds number just increases and cannot decrease.

8.3. GB Natural Inflation

Now, we study the reheating phase in the GB natural inflation model. By using Equation (38), we study the e-folds number and temperature in the reheating phase numerically and find some constraints on these parameters. In this case, the tightest constraint obtained from the base data at 95% CL is $0.525 \leqslant \beta < 1$ (see Table 3). The numerical results corresponding to this constraint are shown in Table 11. The behavior of $N_{\rm rh}$ and $T_{\rm rh}$ versus n_s, for $\beta = 0.7$, is shown in the top panels of Figure 11. As the figure shows, the instantaneous reheating in this case corresponds to $n_s = 0.965$, which is observationally viable.

The bottom panel of Figure 11 shows the range of $N_{\rm rh}$ and $\omega_{\rm eff}$, in the GB natural inflation model, leading to the observationally viable values of the scalar spectral index. As the figure shows, the reheating phase of the universe described by GB natural inflation is not instantaneous. In this case also, the value of $\omega_{\rm eff}$ does not become larger than $\frac{1}{3}$.

8.4. GB α-attractor

To study the reheating phase in the GB α-attractor model, we consider both E-model and T-model types of potential and GB coupling. In the following we present the results for each case.

8.4.1. E-model

In this case we adopt the E-model potential and GB coupling defined in Equation (42). As before, by using these functions, we study the e-folds number and temperature in reheating phase numerically. With E-model potential and GB coupling, the tightest constraint obtained from the base data at 95% CL is $\beta \leqslant 4.81 \times 10^{-2}$. This range of β leads to the constraints presented in Table 12. To obtain these constraints, we have set $\alpha = 50$. The behavior of $N_{\rm rh}$ and $T_{\rm rh}$ versus n_s, for $\beta = 0.03$, is shown in the top and middle panels of Figure 12. In this case, the instantaneous reheating, corresponding to $n_s = 0.965$, is observationally viable. The bottom panel of Figure 12 shows the range of $N_{\rm rh}$ and $\omega_{\rm eff}$ leading to the observationally viable values of the scalar spectral index.

8.4.2. T-model

Now, we consider the T-model potential and GB coupling defined in Equation (47). In this case also, we analyze the e-folds number and temperature in the reheating phase in confrontation with observational data. With T-model potential and GB coupling, the tightest constraint on β, obtained from the base data at 95% CL, is $\beta \leqslant 7.01 \times 10^{-2}$ (see Table 4). The numerical results of the T-model case with $\beta \leqslant 7.01 \times 10^{-2}$ and $\alpha = 50$ are shown in Table 12. The behavior of $N_{\rm rh}$ and $T_{\rm rh}$ versus n_s, for $\beta = 0.03$, is shown in Figure 12. Here also, the instantaneous reheating is favored by observational data. The bottom panel of Figure 12 shows the range of $N_{\rm rh}$ and $\omega_{\rm eff}$, in the case considered in this subsection, leading to the observationally viable values of the scalar spectral index. According to our numerical analysis, in the GB α-attractor model with both E-model and T-model functions, the reheating phase of the universe is not instantaneous and the value of $\omega_{\rm eff}$ does not become larger than $\frac{1}{3}$.

9. Reheating in a GB Model with the Tachyon Field

In this section, we study the reheating process in a GB model with the tachyon field. Here, we can use Equations (88)–(93) of Section 8. However, the energy density and the equation of motion in the tachyon GB model are different from the GB model with a canonical scalar field. In this regard, we have

$$\rho = V\left(1 - \frac{2}{3}\epsilon - \frac{64}{27}\kappa^6 V^2 \alpha'^2 - \frac{8}{3}\kappa^2 \alpha' V'\right)^{-\frac{1}{2}} - \frac{64}{9}\kappa^6 V^2 \alpha'^2 - \frac{8}{3}\kappa^2 \alpha' V'. \quad (100)$$

At the end of inflation ($\epsilon = 1$) we obtain

$$\rho_e = V_e\left(\frac{1}{3} - \frac{64}{27}\kappa^6 V_e^2 \alpha_e'^2 - \frac{8}{3}\kappa^2 \alpha_e' V_e'\right)^{-\frac{1}{2}} - \frac{64}{9}\kappa^6 V_e^2 \alpha_e'^2 - \frac{8}{3}\kappa^2 \alpha_e' V_e'. \quad (101)$$

Now, by using Equations (88) and (101), we reach

$$\rho_{\rm rh} = \left[V_e\left(\frac{1}{3} - \frac{64}{27}\kappa^6 V_e^2 \alpha_e'^2 - \frac{8}{3}\kappa^2 \alpha_e' V_e'\right)^{-\frac{1}{2}} - \frac{64}{9}\kappa^6 V_e^2 \alpha_e'^2 - \frac{8}{3}\kappa^2 \alpha_e' V_e'\right] \times \exp\left[-3N_{\rm rh}(1 + \omega_{\rm eff})\right]. \quad (102)$$

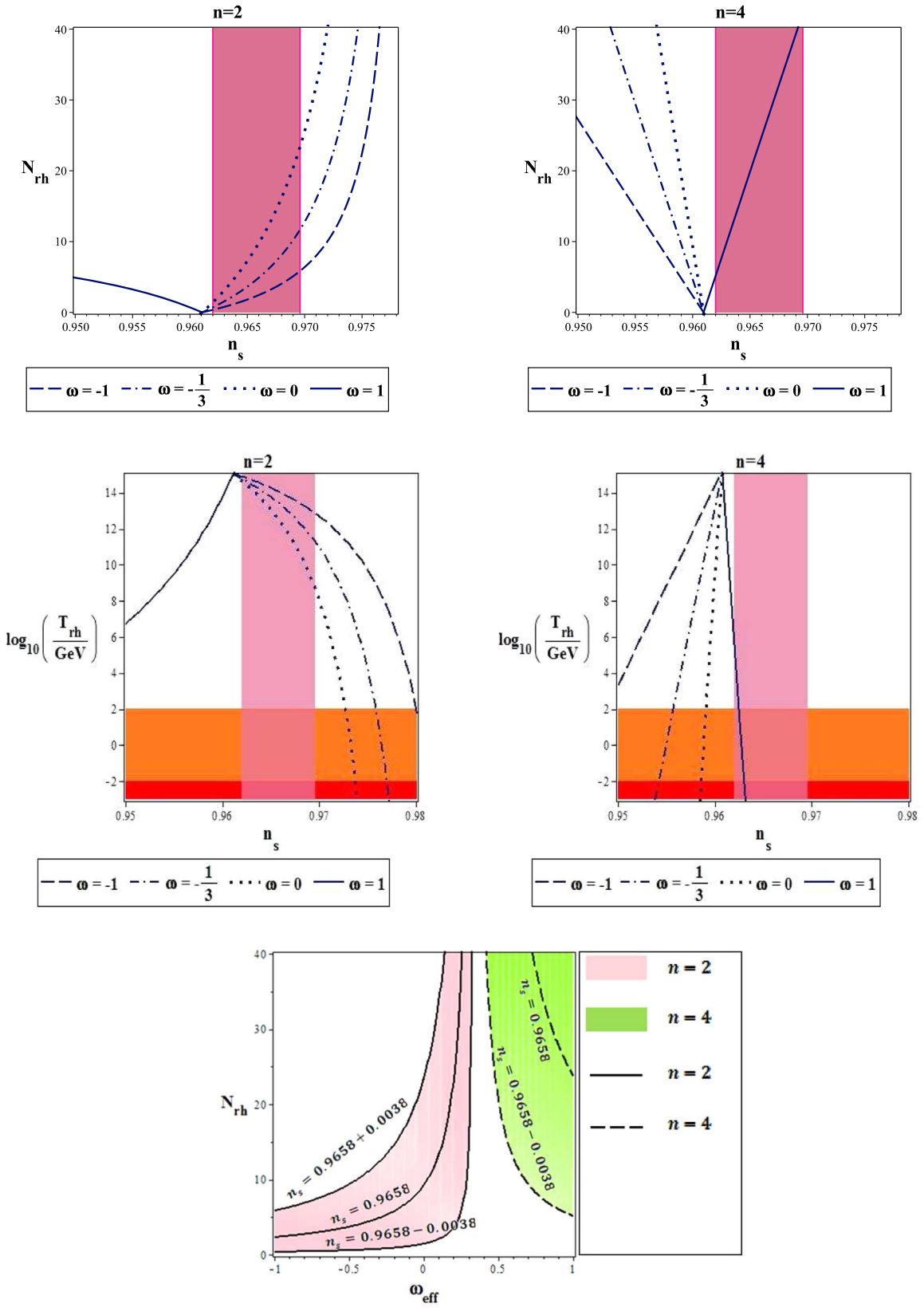

Figure 15. Behavior of the *e*-folds number (top panels) and temperature (middle panels) during the reheating phase vs. the scalar spectral index, and the range of $N_{\rm rh}$ and $\omega_{\rm eff}$ leading to the observationally viable values of the scalar spectral index (bottom panel), in the DBI GB model with $V = V_0\,\phi^n$ and $\mathcal{G} = \mathcal{G}_0\,\phi^{-n}$.

Table 16
Constraints on the e-folds Number and Temperature during the Reheating Phase in the DBI GB Model with $V = V_0\,\phi^n$ and $\mathcal{G} = \mathcal{G}_0\,e^{-\lambda\phi}$, Obtained from Planck2018 TT, TE, EE+lowE+lensing+BK14+BAO Joint Data

		$\omega = -1$	$\omega = -\frac{1}{3}$	$\omega = 0$	$\omega = 1$
$n = 2$	$0.326 \leqslant \beta \leqslant 0.986$	$1.85 \leqslant N_{\rm rh} \leqslant 11.93$	$4.21 \leqslant N_{\rm rh} \leqslant 24.16$	$10.86 \leqslant N_{\rm rh} \leqslant 41.22$	not consistent
$n = 4$	$0.404 \leqslant \beta < 1$	$N \leqslant 5.843$	$N \leqslant 11.45$	$N \leqslant 22.74$	$N \leqslant 10.41$
$n = 2$	$0.326 \leqslant \beta \leqslant 0.986$	$9.03 \leqslant \log_{10}\left(\frac{T_{\rm rh}}{\rm GeV}\right) \leqslant 15.34$	$5.41 \leqslant \log_{10}\left(\frac{T_{\rm rh}}{\rm GeV}\right) \leqslant 13.27$	$0.121 \leqslant \log_{10}\left(\frac{T_{\rm rh}}{\rm GeV}\right) \leqslant 11.02$	not consistent
$n = 4$	$0.404 \leqslant \beta < 1$	$\log_{10}\left(\frac{T_{\rm rh}}{\rm GeV}\right) \geqslant 12.01$	$\log_{10}\left(\frac{T_{\rm rh}}{\rm GeV}\right) \geqslant 7.868$	$\log_{10}\left(\frac{T_{\rm rh}}{\rm GeV}\right) \geqslant 0.442$	$\log_{10}\left(\frac{T_{\rm rh}}{\rm GeV}\right) \geqslant 2.183$

Equations (93) and (102) give the following expression for the scale factor:

$$\ln\left(\frac{a_0}{a_{\rm rh}}\right) = -\frac{1}{3}\ln\left(\frac{43}{11g_{\rm rh}}\right) - \frac{1}{4}\ln\left(\frac{\pi^2 g_{\rm rh}}{30\rho_{\rm rh}}\right) - \ln T_0 - \frac{3}{4}N_{\rm rh}(1+\omega_{\rm eff}) + \frac{1}{4}\ln\left[V_e\left(\frac{1}{3} - \frac{64}{27}\kappa^6 V_e^2\alpha_e'^2 - \frac{8}{3}\kappa^2\alpha_e' V_e'\right)^{-\frac{1}{2}} - \frac{64}{9}\kappa^6 V_e^2\alpha_e'^2 - \frac{8}{3}\kappa^2\alpha_e' V_e'\right]. \quad (103)$$

To find $N_{\rm rh}$, as before, we use $H_{\rm hc}$ obtained from Equation (14). Then, using Equations (90) and (103) gives the e-folds number during the reheating process as follows:

$$N_{\rm rh} = \frac{4}{1-3\omega_{\rm eff}}\left\{-N_{\rm hc} - \ln\left(\frac{k_{\rm hc}}{a_0 T_0}\right) - \frac{1}{4}\ln\left(\frac{40}{\pi^2 g_{\rm rh}}\right) + \frac{1}{2}\ln\left(8\pi^2\mathcal{A}_s\mathcal{W}_s c_s^3\right) - \frac{1}{3}\ln\left(\frac{11g_{\rm rh}}{43}\right) - \frac{1}{4}\ln\left[V_e\left(\frac{1}{3} - \frac{64}{27}\kappa^6 V_e^2\alpha_e'^2 - \frac{8}{3}\kappa^2\alpha_e' V_e'\right)^{-\frac{1}{2}} - \frac{64}{9}\kappa^6 V_e^2\alpha_e'^2 - \frac{8}{3}\kappa^2\alpha_e' V_e'\right]\right\}. \quad (104)$$

From Equations (88), (92), and (101), we get the following expression for the temperature during the reheating process:

$$T_{\rm rh} = \left(\frac{30}{\pi g_{\rm rh}}\right)^{\frac{1}{4}}\left[V_e\left(\frac{1}{3} - \frac{64}{27}\kappa^6 V_e^2\alpha_e'^2 - \frac{8}{3}\kappa^2\alpha_e' V_e'\right)^{-\frac{1}{2}} - \frac{64}{9}\kappa^6 V_e^2\alpha_e'^2 - \frac{8}{3}\kappa^2\alpha_e' V_e'\right] \times \exp\left[-\frac{3}{4}N_{\rm rh}(1+\omega_{\rm eff})\right]. \quad (105)$$

In the following, and to perform a numerical analysis, we adopt the potential and GB function used in Section 6 and explore each case separately.

9.1. Power-law Potential and Inverse Power-law GB Coupling

The first case we consider here is the tachyon GB model with power-law potential and inverse power-law GB coupling (Equation (59)). We find the final values of these adopted functions in terms of the scalar field at the horizon crossing and substitute them in Equations (104) and (105). Then, by obtaining the scalar field at horizon crossing in terms of the scalar spectral index, we rewrite $N_{\rm rh}$ and $T_{\rm rh}$ in terms of n_s and perform a numerical analysis. As demonstrated in Table 5, we have the tightest ranges on β for $n = 2$ as $0.251 \leqslant \beta < 1$ and for $n = 4$ as $0.254 \leqslant \beta < 1$. These ranges of β give the results summarized in Table 13.

The behavior of $N_{\rm rh}$ and $T_{\rm rh}$ versus n_s, for $\beta = 0.7$, is shown in the top and middle panels of Figure 13. As the figure shows, the instantaneous reheating in this case corresponds to $n_s = 0.971$ for $n = 2$ and $n_s = 0.974$ for $n = 4$. Therefore, in this case the instantaneous reheating is not observationally viable. The bottom panel of Figure 13 shows the range of $N_{\rm rh}$ and $\omega_{\rm eff}$, in the case considered in this subsection, leading to the observationally viable values of the scalar spectral index.

9.2. Power-law Potential and Dilaton-like GB Coupling

Now, by using Equation (63), we rewrite the e-folds number and temperature during reheating in terms of the scalar spectral index and perform a numerical analysis on the model. As we see from Figure 6, this model in most ranges of the parameter's space is consistent with observational data. In this case, for the considered sample values of λ, all values of β are observationally viable. However, if we adopt very large values of λ, there would be some constraints on β. For instance, we take $\lambda \sim 10^5$ and find $0.0023 \leqslant \beta < 1$ for $n = 2$ and $0.046 \leqslant \beta < 1$ for $n = 4$. To analyze the reheating phase numerically, we use these ranges of β, which lead to the constraints presented in Table 14.

The behavior of $N_{\rm rh}$ and $T_{\rm rh}$ versus n_s, for $\beta = 0.7$, is shown in Figure 14. As the figure shows, in this case the instantaneous reheating is observationally viable. The bottom panel of Figure 14 shows the range of $N_{\rm rh}$ and $\omega_{\rm eff}$, in the case considered in this subsection, leading to the observationally viable values of the scalar spectral index.

In summary, our study shows that in the tachyon GB model with $V = V_0\,\phi^n$ and $\mathcal{G} = \mathcal{G}_0\,\phi^{-n}$ there is no chance to have $N_{\rm rh} = 0$ in an observationally viable range. Therefore, considering that the reheating phase should start with $N_{\rm rh} = 0$, this model is ruled out. Also, the tachyon GB model with $V = V_0\,\phi^n$ and $\mathcal{G} = \mathcal{G}_0\,e^{-\lambda\phi}$ predicts that by increasing the value of $N_{\rm rh}$, the value of $\omega_{\rm eff}$ increases until it reaches $\frac{1}{3}$. As before, the larger values of $\omega_{\rm eff}$ are not of interest.

10. Reheating in the DBI GB Model

In this section, we study the reheating process in the DBI GB model. Here also, we can use Equations (88)–(93) of Section 8, whereas the energy density and the equation of motion in the DBI

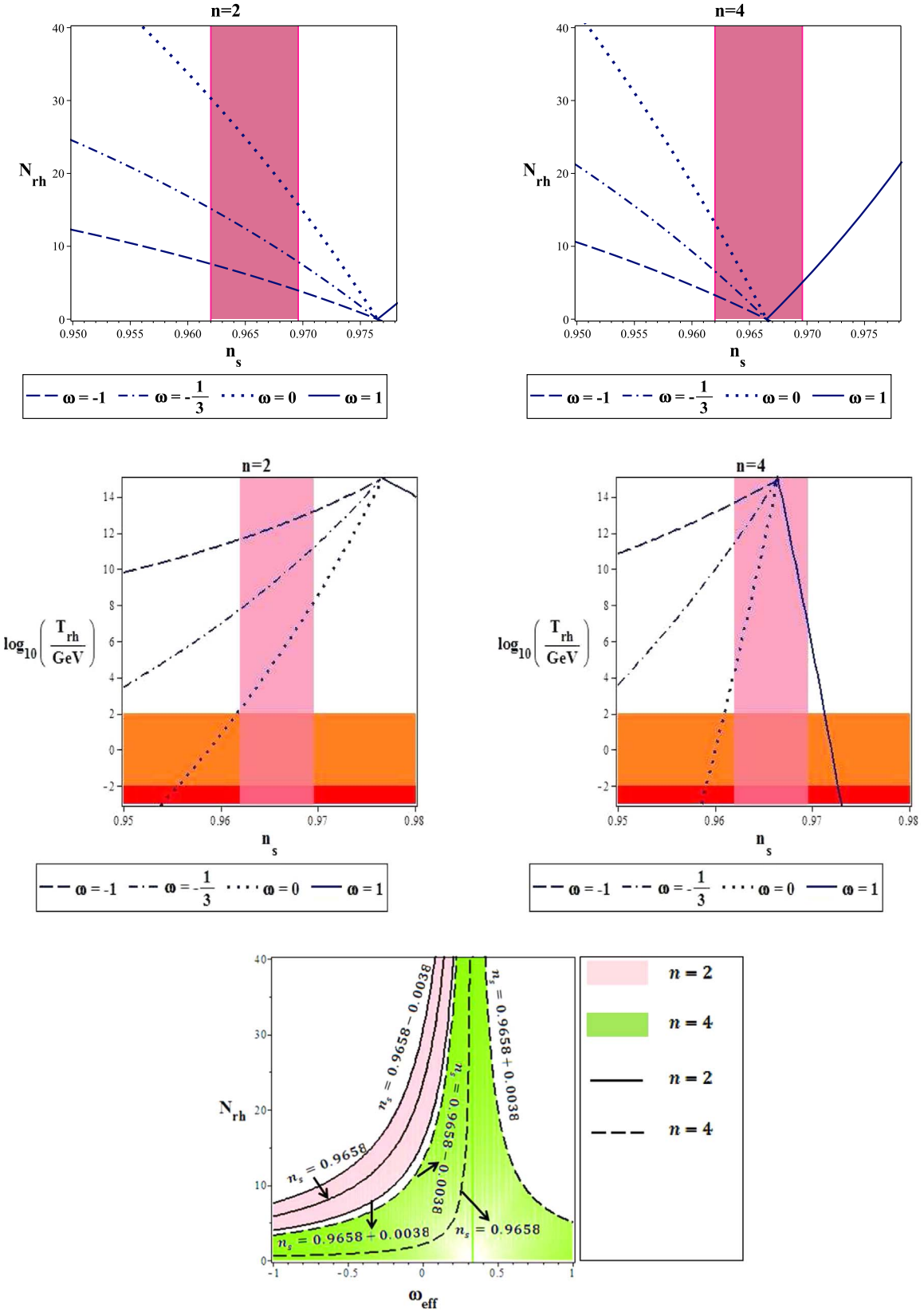

Figure 16. Behavior of the e-folds number (top panels) and temperature (middle panels) during the reheating phase vs. the scalar spectral index, and the range of $N_{\rm rh}$ and $\omega_{\rm eff}$ leading to the observationally viable values of the scalar spectral index (bottom panel), in the DBI GB model with $V = V_0\,\phi^n$ and $\mathcal{G} = \mathcal{G}_0\,e^{-\lambda\phi}$.

GB model are different from those in the GB model with canonical and also tachyon scalar fields. In the DBI GB model we have

$$\rho = f^{-1}\left(1+\frac{2}{3}\epsilon(1+fV)-\frac{64}{27}f\alpha'^2\kappa^4(f^{-1}+V)^3\right)^{-\frac{1}{2}} + V + \frac{8}{3}\alpha'(f^{-1}+V)\left(f'f^{-2}-V'-\frac{8}{3}\kappa^4\alpha'(f^{-1}+V)^2\right). \quad (106)$$

We obtain the following expression at the end of inflation ($\epsilon = 1$):

$$\rho_e = f_e^{-1}\left(1+\frac{2}{3}(1+f_eV_e)-\frac{64}{27}f_e\alpha_e'^2\kappa^4(f_e^{-1}+V_e)^3\right)^{-\frac{1}{2}} + V_e + \frac{8}{3}\alpha_e'(f_e^{-1}+V_e)\left(f_e'f_e^{-2}-V_e'-\frac{8}{3}\kappa^4\alpha_e'(f_e^{-1}+V_e)^2\right). \quad (107)$$

Now, by using Equations (88) and (107), we find the following expression for the energy density during the reheating phase:

$$\rho_{\rm rh} = \left[f_e^{-1}\left(1+\frac{2}{3}(1+f_eV_e)-\frac{64}{27}f_e\alpha_e'^2\kappa^4(f_e^{-1}+V_e)^3\right)^{-\frac{1}{2}} + V_e + \frac{8}{3}\alpha_e'(f_e^{-1}+V_e)\left(f_e'f_e^{-2}-V_e'-\frac{8}{3}\kappa^4\alpha_e'(f_e^{-1}+V_e)^2\right)\right] \times \exp\left[-3N_{\rm rh}(1+\omega_{\rm eff})\right]. \quad (108)$$

From Equations (93) and (108) we reach

$$\ln\left(\frac{a_0}{a_{\rm rh}}\right) = -\frac{1}{3}\ln\left(\frac{43}{11g_{\rm rh}}\right) - \frac{1}{4}\ln\left(\frac{\pi^2 g_{\rm rh}}{30\rho_{\rm rh}}\right) - \ln T_0 - \frac{3}{4}N_{\rm rh}(1+\omega_{\rm eff}) + \frac{1}{4}\ln\left[f_e^{-1}\left(1+\frac{2}{3}(1+f_eV_e)-\frac{64}{27}f_e\alpha_e'^2\kappa^4(f_e^{-1}+V_e)^3\right)^{-\frac{1}{2}} + V_e + \frac{8}{3}\alpha_e'(f_e^{-1}+V_e)\left(f_e'f_e^{-2}-V_e'-\frac{8}{3}\kappa^4\alpha_e'(f_e^{-1}+V_e)^2\right)\right]. \quad (109)$$

Then, by using Equations (90) and (109), we obtain the e-folds number during reheating as follows:

$$N_{\rm rh} = \frac{4}{1-3\omega_{\rm eff}}\left\{-N_{\rm hc} - \ln\left(\frac{k_{\rm hc}}{a_0T_0}\right) - \frac{1}{4}\ln\left(\frac{40}{\pi^2 g_{\rm rh}}\right) + \frac{1}{2}\ln(8\pi^2\mathcal{A}_s\mathcal{W}_sc_s^3) - \frac{1}{3}\ln\left(\frac{11g_{\rm rh}}{43}\right) - \frac{1}{4}\ln\left[f_e^{-1}\left(1+\frac{2}{3}(1+f_eV_e)-\frac{64}{27}f_e\alpha_e'^2\kappa^4(f_e^{-1}+V_e)^3\right)^{-\frac{1}{2}} + V_e + \frac{8}{3}\alpha_e'(f_e^{-1}+V_e)\left(f_e'f_e^{-2}-V_e'-\frac{8}{3}\kappa^4\alpha_e'(f_e^{-1}+V_e)^2\right)\right]\right\}. \quad (110)$$

From Equations (88), (92), and (106), we get the temperature during reheating as follows:

$$T_{\rm rh} = \left(\frac{30}{\pi g_{\rm rh}}\right)^{\frac{1}{4}}\left[V_e\left(\frac{1}{3}-\frac{64}{27}\kappa^6V_e^2\alpha_e'^2-\frac{8}{3}\kappa^2\alpha_e'V_e'\right)^{-\frac{1}{2}} - \frac{64}{9}\kappa^6V_e^2\alpha_e'^2-\frac{8}{3}\kappa^2\alpha_e'V_e'\right] \times \exp\left[-\frac{3}{4}N_{\rm rh}(1+\omega_{\rm eff})\right]. \quad (111)$$

In the following, we study the reheating phase in the DBI GB model numerically.

10.1. Power-law Potential and Inverse Power-law GB Coupling

Here, we adopt power-law potential and inverse power-law GB coupling (Equation (74)) and obtain the final values of these adopted functions in terms of the scalar field at the horizon crossing and substitute in Equations (110) and (111). By obtaining the scalar field at the horizon crossing in terms of the scalar spectral index, we rewrite $N_{\rm rh}$ and $T_{\rm rh}$ in terms of n_s and perform a numerical analysis. As Table 7 shows, we have the tightest range on β as $0.613 \leqslant \beta \leqslant 0.948$ for $n = 2$ and $0.683 \leqslant \beta \leqslant 0.915$ for $n = 4$. In Table 15, we show the observational constraints on $N_{\rm rh}$ and $T_{\rm rh}$, obtained from the mentioned ranges of β.

In the top and middle panels of Figure 15 we see the behavior of $N_{\rm rh}$ and $T_{\rm rh}$ versus n_s, for $\beta = 0.7$. The instantaneous reheating in this case is not observationally viable. The bottom panel of Figure 15 shows the range of $N_{\rm rh}$ and $\omega_{\rm eff}$, in the case considered in this subsection, leading to the observationally viable values of the scalar spectral index.

10.2. Power-law Potential and Dilaton-like GB Coupling

Now, we consider the DBI GB model with power-law potential and dilaton-like GB coupling (Equation (80)). This model in some ranges of the parameter's space is consistent with observational data (see Table 8). In fact, for $n = 2$, we have the tightest range on β as $0.326 \leqslant \beta \leqslant 0.986$, and for $n = 4$ we have $0.404 \leqslant \beta < 1$. By these ranges of β we perform numerical analysis, which gives the constraints shown in Table 16.

The behavior of $N_{\rm rh}$ and $T_{\rm rh}$ versus n_s, for $\beta = 0.6$, is shown in Figure 16. As the figure shows, with $n = 2$ the instantaneous reheating is not observationally viable and with $n = 4$ it is viable. The bottom panel of Figure 16 shows the range of $N_{\rm rh}$ and $\omega_{\rm eff}$, in the case considered in this subsection, leading to the observationally viable values of the scalar spectral index.

According to these numerical considerations, in the DBI GB model with $V = V_0\,\phi^n$ and $\mathcal{G} = \mathcal{G}_0\,\phi^{-n}$, for $n = 2$, there is no chance to have observationally viable $N_{\rm rh} = 0$. Therefore, this case is ruled out. For $n = 4$, the model does not predict $\omega_{\rm eff} \leqslant \frac{1}{3}$ in the observationally viable regions. So, this case is ruled out too. In the DBI GB model with $V = V_0\,\phi^n$ and $\mathcal{G} = \mathcal{G}_0\,e^{-\lambda\phi}$, the case with $n = 2$ is not observationally viable. However, the case with $n = 4$ is consistent with observational data. In fact, this case also predicts that by increasing the value of $N_{\rm rh}$, the value of $\omega_{\rm eff}$ increases until it reaches $\frac{1}{3}$.

11. Summary

In this paper, we have studied inflation and reheating in several GB models. At first, we have considered a general GB model and presented the main equations of the model in the inflation era. In this regard, we have obtained some important perturbation parameters such as the scalar spectral index, tensor spectral index, and tensor-to-scalar ratio. Then, we have considered several GB models and studied the perturbation parameters numerically. By comparing the results with observational data, we have obtained some constraints on the model's parameter space. We have also analyzed the reheating epoch in each model and explored the model's viability in this context too. Our studies give the following results:

1. Although the simple single-field inflation with ϕ^2 potential is not consistent with base and base+GW data sets, considering the GB effect with ϕ^{-2} coupling makes the model with ϕ^2 potential observationally viable. In this case, when the GB effect becomes larger, the tensor-to-scalar ratio becomes smaller and lies in the base data region at 95% CL. We have studied the cases with $N = 50$, $N = 60$, and $N = 70$ for both r–n_s and r–n_T trajectories. The constraint obtained from these studied cases is $0.680 \leqslant \beta < 1$. However, even by including the GB effect, the model with ϕ^4 potential is not observationally viable. We have also analyzed the reheating phase in the simple single-field inflation with ϕ^2 potential. Our analysis shows that, in this model, it is possible to have a viable reheating phase. In the simple single-field inflation with ϕ^2 potential, by increasing $N_{\rm rh}$, the effective equation-of-state parameter changes from -1 and reaches $\frac{1}{3}$, which corresponds to a radiation-dominated era.
2. Considering the GB effect with $e^{-\lambda\phi}$ coupling causes the inflation models with both ϕ^2 and ϕ^4 potentials, in some ranges of the model's parameters, to become consistent with the base data at 95% CL. In this case, have studied the model with $N = 50$, $\lambda = 10$, $\lambda = 10^2$, and $\lambda = 10^4$ for both r–n_s and r–n_T trajectories. When we consider $n = 2$ and $\lambda \lesssim 10^2$, we find the constraint $0.020 \leqslant \beta \leqslant 0.072$, which leads to observational viability of both r–n_s and r–n_T trajectories. However, this constraint is not valid for $n = 2$ and $\lambda > 10^2$. By considering $n = 4$, we have $0.670 \leqslant \beta \leqslant 0.716$. Studying the reheating phase for both cases with $n = 2$ and $n = 4$ shows that in these cases also the effective equation-of-state parameter changes from -1 and reaches $\frac{1}{3}$, which corresponds to a radiation-dominated era.
3. Adding the GB effect to the natural inflation models makes it observationally viable. In this case also the larger values of β lead to smaller values of the tensor-to-scalar ratio. By exploring both r–n_s and r–n_T trajectories for $f = 4$, $f = 15$, $f = 35$, and $f = 60$, we find $0.525 \leqslant \beta < 1$. For the GB natural inflation, analyzing the reheating phase shows that $\omega_{\rm eff}$ in this epoch increases from -1 to $\frac{1}{3}$, which corresponds to a radiation-dominated era. Therefore, this model has the capability to explain the reheating process after inflation.
4. With both E-model and T-model potentials, the inflation models are observationally viable, especially for pretty small values of α. When we consider the GB effect, for any values of α, the larger values of β lead to the smaller values of the tensor-to-scalar ratio. Therefore, the α-attractor GB inflation model is consistent with the base and base+GW data sets at 95% CL too. For both E-model and T-model potentials, studying both r–n_s and r–n_T trajectories gives $\beta \leqslant 4.81 \times 10^{-2}$. In both E-model and T-model cases, it is possible to explain the reheating process. In both cases, the effective equation-of-state parameter change from -1 to $\frac{1}{3}$.
5. Tachyon inflation with ϕ^2 potential is consistent with base data just for $N < 52.7$. By considering the GB effect, this model would be consistent with observational data for $N < 62.4$. The tachyon model with ϕ^4 potential is not consistent with the base and base+GW data sets at all. In this case also, the GB effect causes the model to become observationally viable, for the considered range $50 \leqslant N \leqslant 70$. In both cases, the viability arises because the GB effect makes the tensor-to-scalar ratio of the model smaller. Exploring both r–n_s and r–n_T trajectories gives $0.254 \leqslant \beta < 1$ for $n = 2$ and $0.188 \leqslant \beta < 1$ for $n = 4$. By studying the reheating phase in the tachyon model with ϕ^2 and ϕ^4 potentials, we have found that the reheating epoch cannot be explained in these models. This is because, in these models, the effective equation-of-state parameter does not reach $\frac{1}{3}$ in an observationally viable range of the scalar spectral index.
6. Considering the GB effect with $e^{-\lambda\phi}$ coupling in the tachyon model leads to an observationally viable tachyon model with both ϕ^2 and ϕ^4 potentials. In this case, for smaller values of λ and larger values of β, we have smaller values of tensor-to-scalar ratio, which is consistent with the base and base+GW data. This model with $n = 2$, for $N = 50$, $\lambda = 10$, $\lambda = 10^2$, and $\lambda = 10^4$ for all values of β, is observationally viable. For $n = 4$, and with $N = 50$, $\lambda = 10$, $\lambda = 10^2$, and $\lambda = 10^4$, we have found $0.046 \leqslant \beta$. We have studied the reheating phase in the tachyon model with a dilaton-like GB effect and found that in this case the effective equation-of-state parameter reaches $\frac{1}{3}$. This means that this model has the capability to explain the reheating epoch.
7. DBI inflation with ϕ^2 and ϕ^4 potentials is not consistent with the base and base+GW data sets. However, considering the GB effect with ϕ^{-2} and ϕ^{-4} coupling functions makes the model observationally viable. Note that the DBI model with ϕ^2 potential and ϕ^{-2} GB coupling in some ranges of the model's parameters, is consistent with observational data if $N \geqslant 53.1$. Also, the DBI model with ϕ^4 potential and ϕ^{-4} GB coupling in some ranges of the model's parameters is consistent with observation if $N \geqslant 59.6$. Here also, we have studied the cases with $N = 50$, $N = 60$, and $N = 70$ for both r–n_s and r–n_T trajectories. The constraints obtained from these studied cases are $0.613 \leqslant \beta \leqslant 0.948$ for $n = 2$ and $0.683 \leqslant \beta \leqslant 0.915$ for $n = 4$. Analyzing the reheating phase shows that, in this case, we cannot get the viable reheating process. In fact, with both potentials the effective equation-of-state parameter does not reach $\frac{1}{3}$. Also, with the ϕ^4 potential, this parameter starts with positive values, which is not the case.
8. Considering the GB effect with $e^{-\lambda\phi}$ coupling for the DBI model also leads to the observational viability of the

model with both ϕ^2 and ϕ^4 potentials. As in the previous cases, the GB effect gives a smaller tensor-to-scalar ratio, which is consistent with the different data sets. By exploring both r–n_s and r–n_T trajectories for $f = 4$, $f = 15$, $f = 35$, and $f = 60$, we have found $0.332 \leqslant \beta \leqslant 0.986$ for $n = 2$ and $0.683 \leqslant \beta \leqslant 0.948$ for $n = 4$. The DBI model with ϕ^2 potential and dilaton-like GB coupling loses its viability when we study the reheating phase. This is because the effective equation-of-state parameter in this case does not reach $\frac{1}{3}$. However, the DBI model with ϕ^4 potential and dilaton-like GB coupling has the capability to explain the reheating phase.

We thank the referee for the very insightful comments that have improved the quality of the paper considerably. This work has been supported financially by the Research Institute for Astronomy & Astrophysics of Maragha (RIAAM) under research project No. 1/6025-8.

ORCID iDs

Kourosh Nozari https://orcid.org/0000-0003-4368-5823

References

Abbott, L. F., Farhi, E., & Wise, M. B. 1982, PhLB, 117, 29
Abolhasani, A. A., Firouzjahi, H., & Sheikh-Jabbari, M. 2010, PhRvD, 81, 043524
Adams, F. C., Freese, K., & Guth, A. H. 1991, PhRvD, 43, 965
Ade, P. A. R., Aghanim, N., Armitage-Caplan, C., et al. 2014b, A&A, 571, A22
Ade, P. A. R., Ahmed, Z., Aikin, R. W., et al. 2016, PhRvL, 116, 031302
Ade, P. A. R., Aikin, R. W., Barkats, D., et al. 2014a, PhRvL, 112, 241101
Aghanim, N., Akrami, Y., Ashdown, M., et al. 2018, arXiv:1807.06209
Akrami, Y., Arroja, F., Ashdown, M., et al. 2018, arXiv:1807.06211
Albrecht, A., & Steinhard, P. 1982, PhRvD, 48, 1220
Albrecht, A. J., Steinhardt, P. J., Turner, M. S., & Wilczek, F. 1982, PRL, 48, 1437
Alishahiha, M., Silverstein, E., & Tong, D. 2004, PhRvD, 70, 123505
Andrew, K., Bolen, B., & Middleton, C. A. 2007, GReGr, 39, 2061
Bamba, K., Guo, Z. K., & Ohta, N. 2007, PThPh, 118, 879
Bartolo, N., Komatsu, E., Matarrese, S., & Riotto, A. 2004, PhR, 402, 103
Baumann, D. 2009, arXiv:0907.5424
Boulware, D. G., & Deser, S. 1985, PRL, 55, 2656
Brown, R. A. 2007, PhD thesis, Univ. Portsmouth
Bruck, C. v. d., & Longden, C. 2016, PhRvD, 93, 063519
Burgess, C. P. 2004, LRR, 7, 5
Cai, R.-G., Guo, Z.-K., & Wang, S.-J. 2015, PhRvD, 92, 063506
Campo, S. d., Herrera, R. n, & Toloza, A. 2009, PhRvD, 79, 083507
Cardenas, V. H. 2006, PhRvD, 73, 103512
Cecotti, S., & Kallosh, R. 2014, JHEP, 05, 114
Chen, X. 2010, AdAst, 2010, 638979
Cook, J. L., Dimastrogiovanni, E., Easson, D., & Krauss, L. M. 2015, JCAP, 04, 047
Copeland, E. J., Garousi, M. R., Sami, M., & Tsujikawa, S. 2005, PhRvD, 71, 043003
Dai, L., Kamionkowski, M., & Wang, J. 2014, PRL, 113, 041302
De Felice, A., & Tsujikawa, S. 2011a, JCAP, 1104, 029
De Felice, A., & Tsujikawa, S. 2011b, PhRvD, 84, 083504
Deshamukhya, A., & Panda, S. 2009, IJMPD, 18, 2093
Dine, M., & Kusenko, A. 2004, RvMP, 76, 1
Dolgov, A. D., & Linde, A. D. 1982, PhLB, 116, 329
Dufaux, J. F., Felder, G. N., Kofman, L., Peloso, M., & Podolsky, D. 2006, JCAP, 0607, 006
Elizalde, E., Odintsov, S. D., Pozdeeva, E. O., & Vernov, S. Yu. 2018, IJGMM, 15, 1850188
Feinstein, A. 2002, PhRvD, 66, 063511
Felder, G. N., Garcia-Bellido, J., Greene, P. B., Kofman, L., & Linde, A. D. 2001a, PRL, 87, 011601
Felder, G. N., Kofman, L., & Linde, A. D. 1999, PhRvD, 59, 123523
Felder, G. N., Kofman, L., & Linde, A. D. 2001b, PhRvD, 64, 123517
Ferrara, S., Kallosh, R., Linde, A., & Porrati, M. 2013, PhRvD, 88, 085038
Freese, K., Frieman, J. A., & Olinto, A. V. 1990, PhRvL, 65, 3233
Freese, K., & Kinney, W. H. 2004, PhRvD, 70, 083512
Giudice, G. F., Tkachev, I., & Riotto, A. 1999, JHEP, 9908, 009
Gorini, V., Kamenshchik, A. Y., Moschella, U., & Pasquier, V. 2004, PhRvD, 69, 123512
Greene, B. R., Prokopec, T., & Roos, T. G. 1997, PhRvD, 56, 6484
Gross, D. J., & Sloan, J. H. 1987, NuPhB, 291, 41
Guo, Z. K., & Schwarz, D. J. 2009, PhRvD, 80, 063523
Guo, Z. K., & Schwarz, D. J. 2010, PhRvD, 81, 123520
Guth, A. 1981, PhRvD, 23, 347
Jiang, P.-X., Hu, J.-W., & Guo, Z.-K. 2013, PhRvD, 88, 123508
Joseph, J., Carrasco, M., Kallosh, R., & Linde, A. 2015a, JHEP, 10, 147
Joseph, J., Carrasco, M., Kallosh, R., & Linde, A. 2015b, PhRvD, 92, 063519
Kaiser, D. I., & Sfakianakis, E. I. 2014, PhRvL, 112, 011302
Kallosh, R., & Linde, A. 2013a, JCAP, 1307, 002
Kallosh, R., & Linde, A. 2013b, JCAP, 1312, 006
Kallosh, R., Linde, A., & Roest, D. 2013, JHEP, 1311, 198
Kallosh, R., Linde, A., & Roest, D. 2014a, JHEP, 1408, 052
Kallosh, R., Linde, A., & Roest, D. 2014b, JHEP, 09, 062
Kallosh, R., Linde, A., Roest, D., & Wrase, T. 2016, JCAP, 1611, 046
Kofman, L. 1996, arXiv:astro-ph/9605155
Kofman, L., Linde, A. D., & Starobinsky, A. A. 1994, PRL, 73, 3195
Kofman, L., Linde, A. D., & Starobinsky, A. A. 1997, PhRvD, 56, 3258
Koh, S., Lee, B.-H., Lee, W., & Tumurtushaa, G. 2014, PhRvD, 90, 063527
Koh, S., Lee, B.-H., & Tumurtushaa, G. 2017, PhRvD, 95, 123509
Komatsu, E., Dunkley, J., Nolta, M. R., et al. 2009, ApJS, 180, 330
Liddle, A., & Lyth, D. 2000, Cosmological Inflation and Large-Scale Structure (Cambridge: Cambridge Univ. Press)
Lidsey, J. E., Liddle, A. R., Kolb, E. W., et al. 1997, RvMP, 69, 373
Linde, A. 2015, JCAP, 05, 003
Linde, A. D. 1982, PhLB, 108, 389
Linde, A. D. 1990, Particle Physics and Inflationary Cosmology (Chur: Harwood Academic Publishers)
Lovelock, D. 1971, JMP, 12, 498
Lozanov, K. D., & Amin, M. A. 2014, PhRvD, 90, 083528
Lyth, D. H., & Liddle, A. R. 2009, The Primordial Density Perturbation (Cambridge: Cambridge Univ. Press)
Maldacena, J. M. 2003, JHEP, 0305, 013
Mizuno, S., & Koyama, K. 2010, PhRvD, 82, 103518
Mukhanov, V. F., Feldman, H. A., & Brandenberger, R. H. 1992, PhR, 215, 203
Munoz, J. B., & Kamionkowski, M. 2015, PhRvD, 91, 043521
Nojiri, S., & Odintsov, S. D. 2005, PhLB, 631, 1
Nojiri, S., & Odintsov, S. D. 2011, PhR, 505, 59
Nojiri, S., Odintsov, S. D., & Oikonomou, V. K. 2017, PhR, 692, 1
Nojiri, S., Odintsov, S. D., Oikonomou, V. K., Chatzarakis, N., & Paul, T. 2019, EPJC, 79, 565
Nojiri, S., Odintsov, S. D., & Sasaki, M. 2005, PRD, 71, 123509
Nojiri, S., Odintsov, S. D., & Tretyakov, P. V. 2007, PhLB, 651, 224
Nozari, K., & Fazlpour, B. 2008, JCAP, 0806, 032
Nozari, K., & Rashidi, N. 2009a, IJTP, 48, 2800
Nozari, K., & Rashidi, N. 2009b, JCAP, 0909, 014
Nozari, K., & Rashidi, N. 2009c, IJMPD, 19, 219
Nozari, K., & Rashidi, N. 2013a, PhRvD, 88, 023519
Nozari, K., & Rashidi, N. 2013b, PhRvD, 88, 084040
Nozari, K., & Rashidi, N. 2014, PhRvD, 90, 043522
Nozari, K., & Rashidi, N. 2016a, Adv. High Energy Phys., 2016, 1252689
Nozari, K., & Rashidi, N. 2016b, PhRvD, 93, 124022
Nozari, K., & Rashidi, N. 2017, PhRvD, 95, 123518
Nozari, K., & Rashidi, N. 2018, ApJ, 863, 133
Nozari, K., & Rashidi, N. 2019, ApJ, 882, 78
Odintsov, S. D., & Oikonomou, V. K. 2016, PhRvD, 94, 124026
Odintsov, S. D., & Oikonomou, V. K. 2018, PhRvD, 98, 044039
Odintsov, S. D., Oikonomou, V. K., & Banerjee, S. 2019, NuPhB, 938, 935
Padmanabhan, T. 2002, PhRvD, 66, 021301
Rashidi, N., & Nozari, K. 2018, IJMPD, 27, 1850076
Rashidi, N., Nozari, K., & GrØn, Ø. 2018, JCAP, 05, 044
Riotto, A. 2002, arXiv:hep-ph/0210162
Sami, M., Chingangbam, P., & Qureshi, T. 2002, PhRvD, 66, 043530
Sen, A. 1999, JHEP, 10, 008
Sen, A. 2002a, JHEP, 07, 065

Sen, A. 2002b, MPLA, 17, 1797
Shahalam, M., Myrzakulov, R., Myrzakul, S., & Wang, A. 2018, IJMPD, 27, 1850058
Shuhmaher, N., & Brandenberger, R. 2006, PhRvD, 73, 043519
Silverstein, E., & Tong, D. 2004, PhRvD, 70, 103505
Spalinski, M. 2007, JCAP, 0705, 017
Traschen, J. H., & Brandenberger, R. H. 1990, PhRvD, 42, 2491
Ueno, Y., & Yamamoto, K. 2016, PhRvD, 93, 083524
Wallisch, B. 2018, PhD thesis, Cambridge Univ.
Wu, Q., Zhu, T., & Wang, A. 2018, PhRvD, 97, 103502
Yi, Z., Gong, Y., & Sabir, M. 2018, PhRvD, 98, 083521
Zwiebach, B. 1985, PhLB, 156, 315